Boudin, F., Allgeyer, S., Bernard, P., Hébert, H., Olcay, M., Madariaga, R., El-Madani, M., Vilotte, J. P., Peyrat, S., Nercessian, A., Schurr, B., Esnoult, M. F., Asch, G., Nunez, I., Kammenthaler, M. (2013): Analysis and modelling of tsunami-induced tilt for the 2007, M = 7.6, Tocopilla and the 2010, M = 8.8 Maule earthquakes, Chile, from long-base tiltmeter and broadband seismometer records. - Geophysical Journal International, 194, 1, pp. 269—288.

DOI: http://doi.org/10.1093/gji/ggt123

Geophysical Journal International

Geophys. J. Int. (2013) **194,** 269–288
Advance Access publication 2013 April 28

doi: 10.1093/gji/ggt123

Analysis and modelling of tsunami-induced tilt for the 2007, $M = 7.6$, Tocopilla and the 2010, $M = 8.8$ Maule earthquakes, Chile, from long-base tiltmeter and broadband seismometer records

F. Boudin,[1] S. Allgeyer,[2] P. Bernard,[3] H. Hébert,[4] M. Olcay,[5] R. Madariaga,[2] M. El-Madani,[3] J.-P. Vilotte,[3] S. Peyrat,[1] A. Nercessian,[3] B. Schurr,[6] M.-F. Esnoult,[3] G. Asch,[6] I. Nunez[5] and M. Kammenthaler[7]

[1] *Géosciences Montpellier, Place Eugène bataillon,* 34095 *Montpellier, France. E-mail: boudin@gm.univ-montp2.fr*
[2] *Ecole Normale supérieure de Paris,* 45, *rue d'Ulm,* 75230 *Paris cedex* 05, *France*
[3] *Equipe de Sismologie, Institut de Physique du Globe de Paris,* 1 *rue Jussieu,* 75252 *Paris Cedex* 05, *France*
[4] *CEA, DAM,DIF,* F-91297, *Arpajon, France*
[5] *Universidad Arturo Prat, Iquique, Chile*
[6] *Helmholtz Centre Potsdam, GFZ German Research Centre for Geosciences, Telegrafenberg,* 14473 *Potsdam, Germany*
[7] *Spéléo Secours Français Alsace,* 32 *rue Charles-Marie Widor,* 68000 *Colmar, France*

Accepted 2013 March 26. Received 2013 March 20; in original form 2012 June 13

SUMMARY

We present a detailed study of tsunami-induced tilt at in-land sites, to test the interest and feasibility of such analysis for tsunami detection and modelling. We studied tiltmeter and broadband seismometer records of northern Chile, detecting a clear signature of the tsunamis generated by the 2007 Tocopilla ($M = 7.6$) and the 2010 Maule ($M = 8.8$) earthquakes. We find that these records are dominated by the tilt due to the elastic loading of the oceanic floor, with a small effect of the horizontal gravitational attraction. We modelled the Maule tsunami using the seismic source model proposed by Delouis *et al.* and a bathymetric map, correctly fitting three tide gauge records of the area (Antofagasta, Iquique and Arica). At all the closest stations (7 STS2, 2 long-base tiltmeters), we correctly modelled the first few hours of the tilt signal for the Maule tsunami. The only phase mismatch is for the site that is closer to the ocean. We find a tilt response of 0.005–0.01 μm at 7 km away from the coastline in response to a sea level amplitude change of 10 cm. For the Maule earthquake, we observe a clear tilt signal starting 20 min before the arrival time of the tsunami at the nearest point on the coastline. This capability of tilt or seismic sensors to detect distant tsunamis before they arrive has been successfully tested with a scenario megathrust in the southern Peru-northern Chile seismic gap. However, for large events near the stations, this analysis may no longer be feasible, due to the large amplitude of the long-period seismic signals expected to obscure the loading signal. Inland tilt measurements of tsunamis smooth out short, often unmodelled wavelengths of the sea level perturbation, thus providing robust, large-scale images of the tsunami. Furthermore, tilt measurements are not expected to saturate even for the largest run-ups, nor to suffer from near-coast tsunami damages. Tiltmeters and broadband seismometers are thus valuable instruments for monitoring tsunamis in complement with tide gauge arrays.

Key words: Sea level change; Transient deformation; Earth rotation variations; Tsunamis; Elasticity and anelasticity; Lithospheric flexure.

1 INTRODUCTION

A large tsunami was generated by the Mw8.8, Maule earthquake of 2010 February 27 in Central Chile (Fritz *et al.* 2011; Vigny *et al.* 2011). It was the strongest tsunami in the Southern Pacific Ocean since 1960, when a Mw9.5 broke a 1000-km long segment of the Chilean subduction located to the south of the Maule event (Plafker & Savage 1970). The last megathrust earthquake in the Conception–Constitution region before the 2010 event occurred in 1835 (Darwin 1851). The 2010 Maule earthquake claimed 521 deaths and 124 caused by the Tsunami in the epicentral region, which extended over 400 km in the north–south direction.

Another seismic gap, in northern Chile and southern Peru, has a potential rupture length of many hundred kilometres between

the cities of Arequipa in Peru and Arica in Chile. The two last megathrust earthquakes in this region, with magnitudes close to 9, occurred more than 130 yr ago: in 1868 in southern Peru (Dorbath *et al.* 1990; Comte & Pardo 1991), stopping close to Arica to the south. The other occurred in 1877 in northern Chile, breaking a 600 km stretch of the subduction zone between Arica and Antofagasta. GPS data by (Angermann *et al.* 1999; Chlieh *et al.* 2004) show strong interplate coupling in this gap so that we may infer that the 7 cm yr^{-1} convergence rate between the Nazca and the South america plate is stored elastically since the nineteenth century megathrusts, leading to a potential of about 10 m slip for the next large event. Such an event would reach a magnitude between 8.0 and 9.0.

The threat of such an event in northern Chile and the need to better monitor and understand the seismic and strain activity of the region before the expected megathrust rupture lead to the International Plate Boundary Observatory (IPOC) project. It started in 2005, with the installation of a backbone array of observations sites, from Antofagasta to Arica, with broadband seismometers, continuous GPS and tiltmeters, completing the tidal gauge network of SHOA (Servicio Hidrografico Oceanografico de la Armada).

The southern part of this gap was struck in 2007 by the $M = 7.7$ Tocopilla, interplate thrust earthquake. This event did not relieve much of the accumulated elastic strain, due to its confinement in the deepest part of the interplate interface (Peyrat *et al.* 2010). It produced some small tsunami waves of few tens of centimetres, which were recorded by the tide gauges of Arica, Iquique and Antofagasta.

The 2010 Maule tsunami produced large waves at these sites of the order of 50 cm to 1 m. For both events, a careful processing and analysis of the long-base tiltmeters (LBTs) and the STS2 seismometer records of IPOC revealed horizontal long-period signals, lasting several days after the events, which could be unambiguously correlated with the tide gauge records and the tsunamis waves. Observations of tsunami effect on horizontal broadband seismometers records were already reported in the Indian Ocean and in Japan for the 2004 Sumatra tsunami (Yuan *et al.* 2005; Nawa *et al.* 2007); for submarine landslide in the Fram Strait (Berndt *et al.* 2009) and for the 2003 large landslide on the Stromboli volcano (Pino *et al.* 2004). However, no quantitative modelling of these effects has been attempted, and, in particular, the contributions on tilt, by the classical surface loading effect for an elastic body, and of the direct gravitational perturbation by the water mass were not estimated. Whatever the details of the mechanism, tilt records provide, of way of weighting the excess or deficiency of oceanic water mass, which produces spatially smoothed and non-local information which is possibly different from that of the local sea level monitored by tide gauges, as pointed out by (Bernard *et al.* 2004). Note that the tilt (Blum & Hatzfeld 1970) induced by sea level change was reported long ago at tidal periods, with tiltmeters and GPS (Vergnolle *et al.* 2008; Williams & Penna 2011), and has recently been used in a quantitative way at a large scale to constrain the density and elastic constants of the Earth (Ito & Simons 2011).

The aim of the present study is to demonstrate the feasibility of quantitatively modelling the near-coastal tilt signals due to the first waves of a tsunami, using records of the 2007 and 2010 Chilean tsunamis. We also want to assess the potential use of near-coast tiltmeters and broadband seismometers for the detection the incoming tsunamis.

In the following, we first present the observational evidence of tsunami-induced tilt for the 2007 and 2010 events. For the 2010 Maule earthquake, we then define and quantify the physical processes contributing to this effect, using a tsunami model. We calculate the induced tilt and acceleration signals at the broadband seismometer and LBTs and compare them to the observations. Finally, we analyse the starting phase of the tsunami-induced signal, which we compare to the tide gauge records to determine their relative arrival times: we do this for the 2010 Maule records, and for synthetic records of a simulated megathrust event in southern Peru.

2 IPOC SITES AND RECORDING CHARACTERISTICS OF SEISMIC, TILT AND SEA-TIDE SENSORS

In the frame of the IPOC program (Integrated Plate boundary Observatory Chile, http://www.ipoc-network.org), an observatory was installed in northern Chile to study the 600-km long seismic gap between Antofagasta and Arica. The partners of this project are IPGP, GFZ-Potsdam, CNRS-INSU and the University of Chile. Fourteen multiparameter stations were installed, each station having a broadband seismometer, accelerometer, GPS antenna and four of them had a short-base tiltmeter (pendulum). In addition, two sites near Iquique were equipped with long baseline, hydrostatic tiltmeters (LBTs). In the present study, we use the seismic stations close to the sea and the two LBTs (see Fig. 1 and Table 1). Distances from the station to the seashore vary from 2.8 km (PAT) and 2.1 km (PB10) for the closest site, to 28 km (HMB) for the farthest. Station LVC, from the GEOFON array, at 150 km from the coast, is also considered for reference. The two LBT sites (Neuquen and Santa Rosa) are 7 and 10 km away from the coastline, respectively.

The long-base hydrostatic tiltmeters were installed to continuously monitor the interseismic low-frequency strain or tilt signals, with a resolution better than the GPS. Indeed, when properly installed at an adequate underground site, long-base titmeters can achieve a very high long-term stability (tilt drift possibly smaller than 10^{-7} rad yr^{-1}) and a short-term high-resolution equivalent to 10^{-9} rad (Kostoglodov *et al*. 2002; d'Oreye & Zürn 2005; Boudin *et al.* 2008). Short-base tiltmeters and borehole tiltmeters do not usually reach a long-term stability better than 1 μrad yr^{-1}. Our LBT sensors in northern Chile work with water tubes according to the standard hydrostatic levelling system (Boudin *et al.* 2008). When the baseline tilts, the liquid moves from one vessel to another to allow the levelling between the two vessels. They are installed underground in horizontal tunnels of two old mines, providing stable bedrock for a proper coupling at both ends of the instruments, as well as good thermal insulation (Fig. 2). The Neuquen and Santa Rosa tiltmeters were installed in 2007 and 2009 at depths of 30 and 150 m below the surface and their lengths are 38 and 51 m, respectively. The tilt signal is recorded on a 18 bits DataTaker logger dt80 at the sampling rate of 1/30 s. Note that the long water tube has a physical low pass, filtering effect at 3 min period (5 mHz), due to water viscosity (Boudin *et al.* 2008).

The STS2 seismometers from IPOC are also located underground, but much closer to the surface, at 2 or 3 m depth inside small tunnels which were excavated in the bedrock for this purpose. This shallow depth proved to be sufficient to detect tsunami tilt because of the shorter period of tsunami waves (hour) with respect to the dominant diurnal signals of thermal stresses. The seismic signal is recorded on a 26 bits Quanterra logger, and we use the 1 Hz sampling rate channel (LH). The tide gauges of Iquique, Antofagasta and Arica, all located in the sheltered water of the main harbours, have a sampling rate of 2 min and a resolution of a few millimetres (more information can be found at http://www.ioc-sealevelmonitoring.org/).

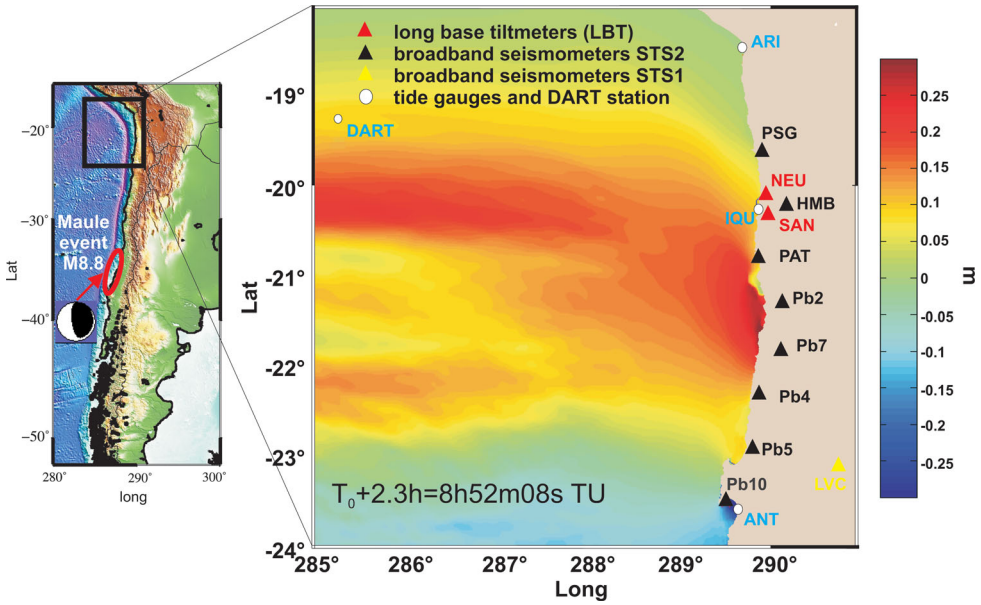

Figure 1. Map of the IPOC sites and snapshot of the Maule 2010 tsunami model. (Left) Location of the Maule earthquake (red ellipse) and of the study area (rectangle). (Right) Map of the IPOC stations (composed of some LBT and STS2 sensors), the GEOFON-LVC station (an STS1 sensor) and the tide gauges of SHOA (details on symbols described at top of figure). Water height is calculated at 2.3 h after the origin time (= 8:52:08 UT). Colour code of tsunami amplitude is in metre.

Table 1. Geographical coordinates of the stations of the IPOC network.

Name	Lat (°)	Long (°)	Alt (m)	Distance from the coast (km)
NEUQUEN (NEU)	−20.17183	−70.07352	1045	7
SANTA ROSA (SAN)	−20.28722	−70.04423	960	9.3
HMB	−20.27822	−69.88791	1152	26.5
Patache (PAT)	−20.82071	−70.15288	832	3
Pisagua (PSG)	−19.59717	−70.12305	966	9.4
PB02	−21.31970	−69.89600	1015	18
PB04	−22.33350	−70.14939	1520	10.5
PB05	−22.86790	−70.18590	1150	11
PB07	−21.72660	−69.88610	1570	28.7
PB10	−23.51240	−70.55410	250	2.1
LVC	−22.61820	−68.91130	2915	137

3 FIRST OBSERVATION OF TILT INDUCED BY THE 2007 TOCOPILLA TSUNAMI

The $M = 7.7$ Tocopilla earthquake occurred on 2007 November 14 at 15:40:50 UTC. From IPOC seismic records, the hypocentre was located at 69.869°W and 22.204°S and 40 km depth (Delouis *et al.* 2009; Peyrat *et al.* 2010). The 200 km north from the epicentre, about 1 hr later, the records of the LBT at Neuquen showed the beginning of clear oscillations (Fig. 3), very similar to the long-period signals ($T > 1000$ s) of the nearby tide gauge of Iquique, but also with some delay of Antofagasta and Arica. The seismic signal of the main shocks is clearly seen on the STS2 unfiltered records of Fig. 3.

We interpret this tilt signal as the load and gravity effect of the tsunamis waves passing near Neuquen. On the closest tide gauge, at Iquique, the first tsunami waves had an amplitude of about 10 cm, and the following oscillations have a characteristic period of 43 min which persists during more than 1 d.

A spectral analysis of six records (tilt of LBT, tilt of two STS2 and three tide gauges), for a duration of 32 hr, is presented in Fig. 4(a),

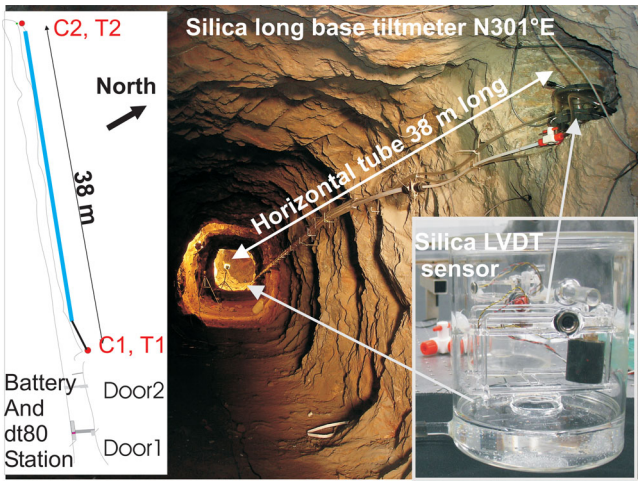

Figure 2. LBT at the Neuquen site in northern Chile. (Left) Map view of the LBT installation in the mine. The blue line shows the position of the 38 m long, horizontal water tube. Red dots indicate the water levelling systems with silica sensors. On the right, we show a picture of the installation, as seen from C1. (Insert, right) Picture of the silica levelling sensor.

showing at all sites of the large peak at 43 min eigenperiod. At smaller periods, between 5 and 20 min, the spectrum at the Iquique tidal gauge shows more energy than at the LBT station, most probably due to local resonances in the harbour (Sahal *et al.* 2009), which cannot be detected at LBT because of the averaging effect of distance for small-scale loading sources with zero mean value. Between 5 and 35 min, the spectral noise at the STS2s station is higher than at the LBT station, due to the high amplitude of low-frequency local atmospheric pressure effect. These effects do not appear on the Neuquen site because the large dimension of the LBT reduces the local atmospheric pressure effects. The clear spectral record of the tsunami signal on the tiltmeter (Fig. 4a) can also be observed as a 10 nrad (1 nrad = 10^{-9} radians) oscillation on the

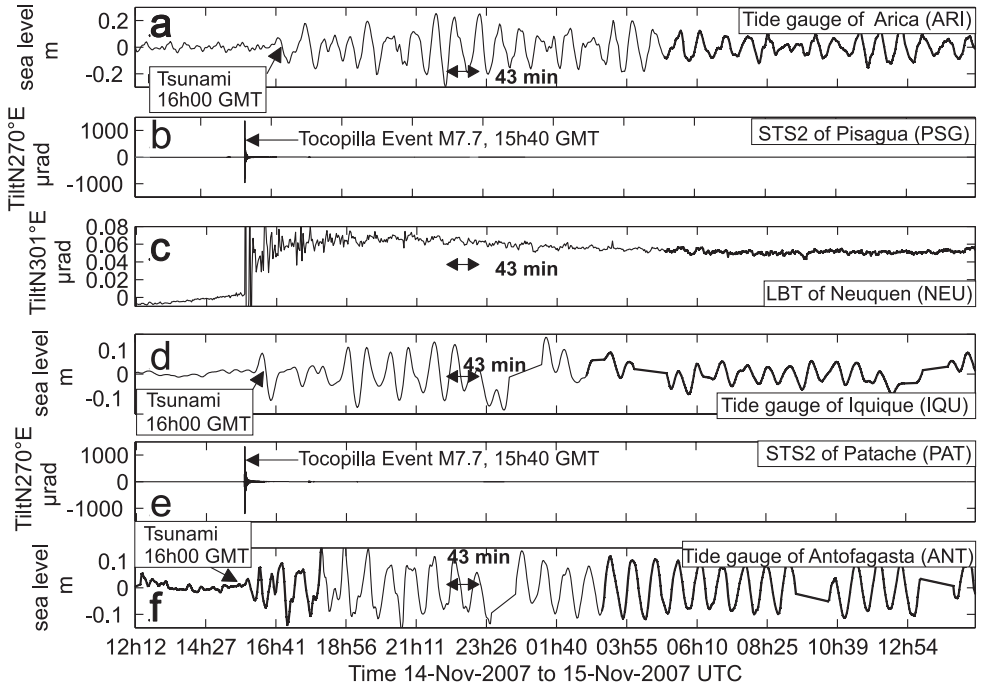

Figure 3. Ground tilt, seismic and sea level records of the Mw7.7 Tocopilla 2007 earthquake. Tidal data at Arica (a), Iquique (d) and Antofagasta (f) are from SHOA. STS2 records deconvolved from the instrument are shown at Pisagua (b) and Patache (e). The N121° tilt LBT record at Neuquen is shown in (c).

bandpass filtered signal between 800 s and 3 hr presented in Fig. 5. We used a Butterworth filter of order 2 (zero-phase acausal). This is a zero-phase forward and reverse digital filter. The tsunami signal is more difficult to detect on the PAT and PSG STS2 sites due to low-frequency noise.

We propose that this 43 min resonance is due to shallow water gravity waves trapped between the coast and the trench. Due the increase of tsunami velocity with the water depth h (as $h^{1/2}$), the shallow depth coastal band acts as a low-velocity zone for the tsunami wave, trapping the energy away from the deep, high-velocity oceanic layer located more to the west beyond the trench. This effect is stronger for waves which are generated close to the coast and whose take-off angle from the coast is small. This is very similar, in the case of an elastic solid body, to surface waves generated by sources within the low-velocity layer. The existence of this resonance at Iquique is clearly observed outside the time windows of the studied tsunamis, as evidenced in Fig. 4(b) where we analyse the record of the month of February, just before the Maule earthquake. Note that from the tsunami records, this resonant period is surprisingly stable over the 600 km of monitored coastline, which can be explained by the similarity of the bathymetric profile. This is consistent with a detailed analysis of such resonances effects on tide gages presented by (Yamazaki & Cheung 2011) for the Maule Earthquake: they observed resonance peaks between 35 and 129 min and also showed that the resonances are largely independent of the tsunami source.

On the bandpass filtered tilt record of Fig. 5(b), 20 min after the first arrival of the seismic signals, at a time when the seismic coda is significantly reduced, a clear positive pulse of several tens of minute duration is observed in coincidence with the first tsunami wave detected at Iquique. We thus suggest that this 10 nrad signal is indeed the tilt response to the first tsunami wave. As the tsunami waves propagate towards the north, the location of the Neuquen station 7 km to the north of Iquique (Fig. 2) as well as its maximal tilt sensitivity to water loading masses located to the NW (N301°E tilt) both imply a later arrival of the tsunami signal at Neuquen with respect to Iquique, consistent with the detected delay of about 3 min.

Finally, we infer from the above observations that for the Tocopilla earthquake, a tiltmeter station closer to the epicentral region (say at 100 km instead of 200 km) may not have shown a detectable tsunami-induced tilt signal, because this signal would have been buried in a much earlier and stronger seismic coda due to the shorter propagation time of the tsunami (20 min instead of 40 min).

4 TILTMETER AND STS2 RECORDS OF THE 2010 MAULE TSUNAMI

4.1 Observation on the LBTs

The $M = 8.8$ Maule earthquake occurred at 6h34m14.5s UTC on 2010 February 27 and was located at 72.898°W and 36.122°S (Vigny *et al.* 2011). The sea level rose several metres in the epicentral area (Fritz *et al.* 2011), reaching 4 m in Valparaiso, 50 km north from the northern end of the rupture. In northern Chile, at more than 1800 km from the epicentre, the tide gauges of Antofagasta, Iquique and Arica operated by SHOA recorded a 0.5–2-m sea level change (see records at Iquique in Fig. 6c).

The signal to noise ratio of the tsunami records appeared to be larger than for the Tocopilla event, which motivated our attempt for a quantitative modelling. The sea level variation at Iquique was indeed about 2.5 times larger for this tsunami than for the 2007 Tocopilla event. Furthermore, the first tsunami wave for Maule arrived 2.5 hr after the start of the seismic event, and therefore after the high noise time window of the large-amplitude, long-period seismic waves.

We present the tilt records of the two LBTs of Neuquen and Santa Rosa stations in Figs 6(a) and (b), along with the Iquique tide gauge record (Fig. 6c). The tilt, sampled at 1/30 s, is filtered with a

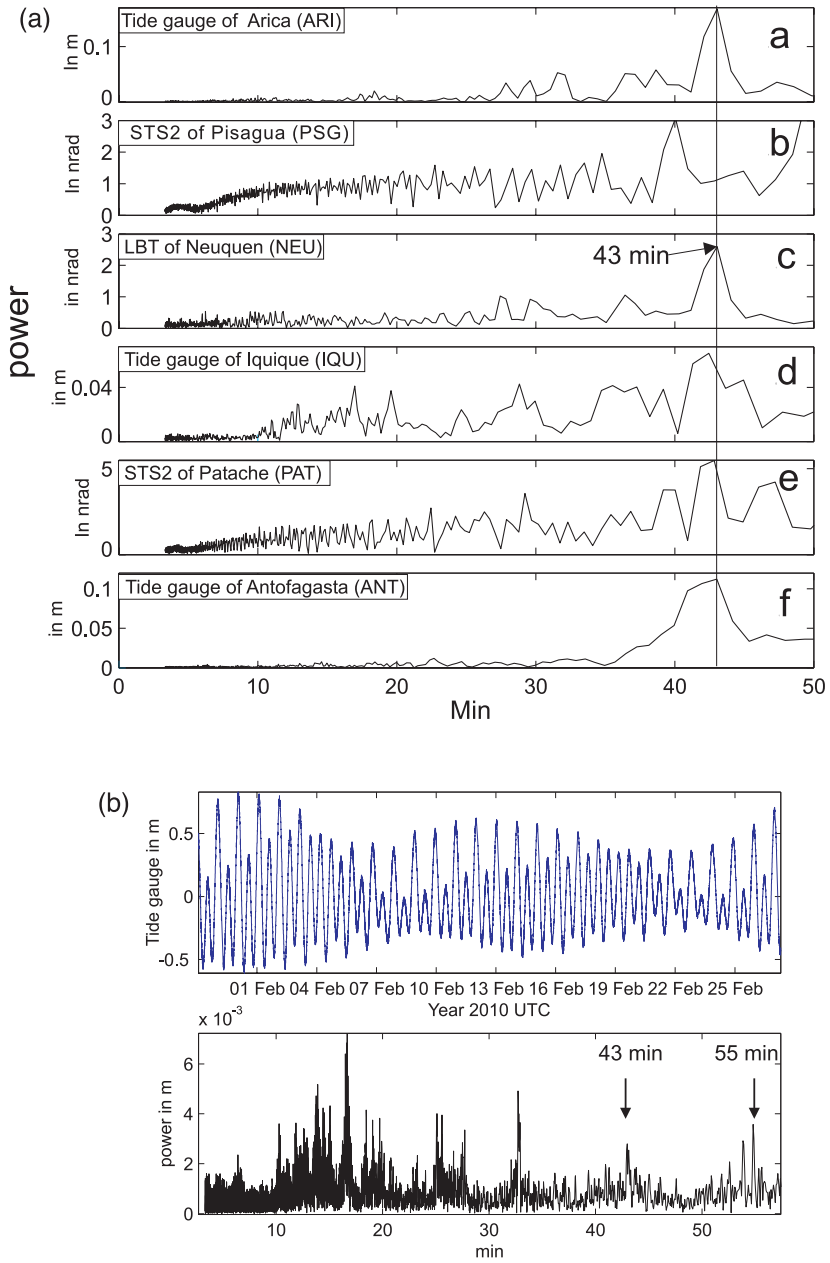

Figure 4. (a) Comparison of spectra of the tilt and sea level for the Tocopilla 2007 event. Power spectra of the 24 hr of Fig. 3 for the tilt at Neuquen (a) and for the three tide gauges of Arica, Iquique and Antofagasta (b). The large, common resonant peak at 43 min corresponds to oceanic gravity waves trapped near the coast. (b) Data of the February 2010 sea level record at Iquique (IQUI) (top) before the Maule Event the 27 February 2010. (Bottom) Spectral analysis of this record, with a zoom on the period range from 1 to 57 min.

moving average of six points, and the tide gauge, sampled at 1/60 s, is filtered on three points, to have an equivalent filter. The first tsunami wave and the corresponding tilt on both instruments clearly appear at around 8:50, followed by a persistent oscillation, on the three records, related to a resonance effect, similar to that observed for the Tocopilla event. There is, however, a clear difference between the sea level and the tilt records in terms of frequency content of these oscillations, which will be discussed later.

We note from Fig. 6 and from the zoom in Fig. 7 that the LBT Neuquen and Santa Rosa tilt records are very well correlated in phase and amplitude. This is due to the similar azimuth of tilt measurement, respectively, 301°E and 330°E, and to the small inter-site distance of 14 km in comparison to the tsunami wavelengths. Fig. 7 also shows a striking similarity in phase between the tilt and the tidal records, at the lowest frequencies. In Fig. 7 (top), the tilt records are dominated by the long-period resonance of the sea level between 40 and 60 min. They do not show as much high frequencies as in the tide gauge records in Fig. 7 (bottom). This is due to the averaging effect, over tens of kilometres, of the distributed sources of load, smoothing out the effect of small-scale sea level fluctuations.

4.2 Observation on broadband seismometer STS2

The apparent horizontal acceleration due to the horizontal component of gravity g can be clearly recorded on broadband

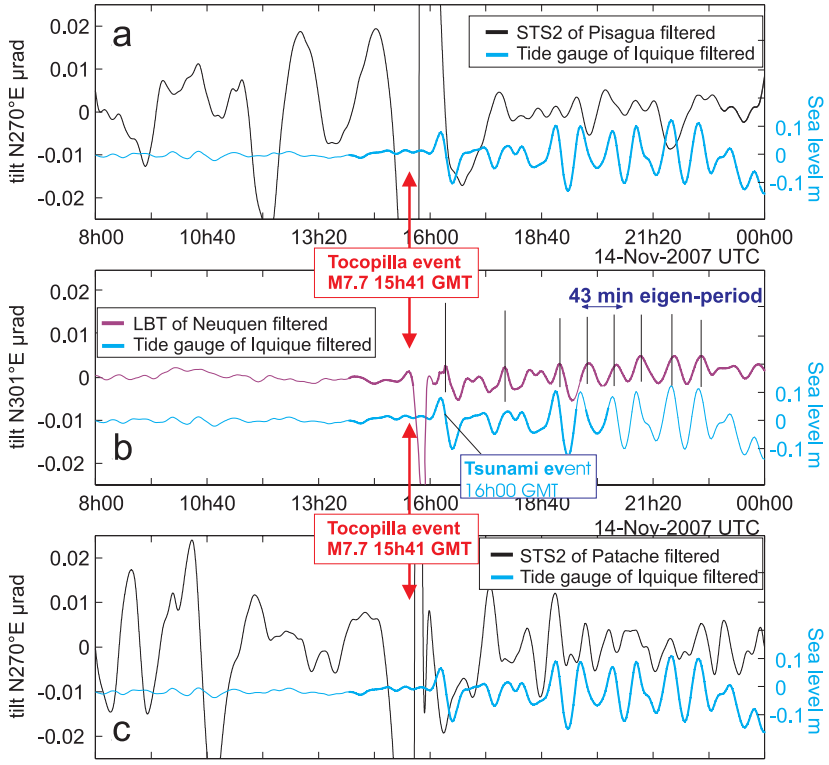

Figure 5. Comparison between the sea level at Iquique and the low noises level on the tilt of Pisagua (a), Neuquen (b) and Patache (c) station for the 2007 Tocopilla earthquake. We have applied a Butterworth filter of order 2 (zero-phase, acausal) with bandpass filtered between 800 s and 3 hr. In (b), vertical bars indicate peaks in the tilt most of which are delayed by about 5 min with respect to peaks on the sea level.

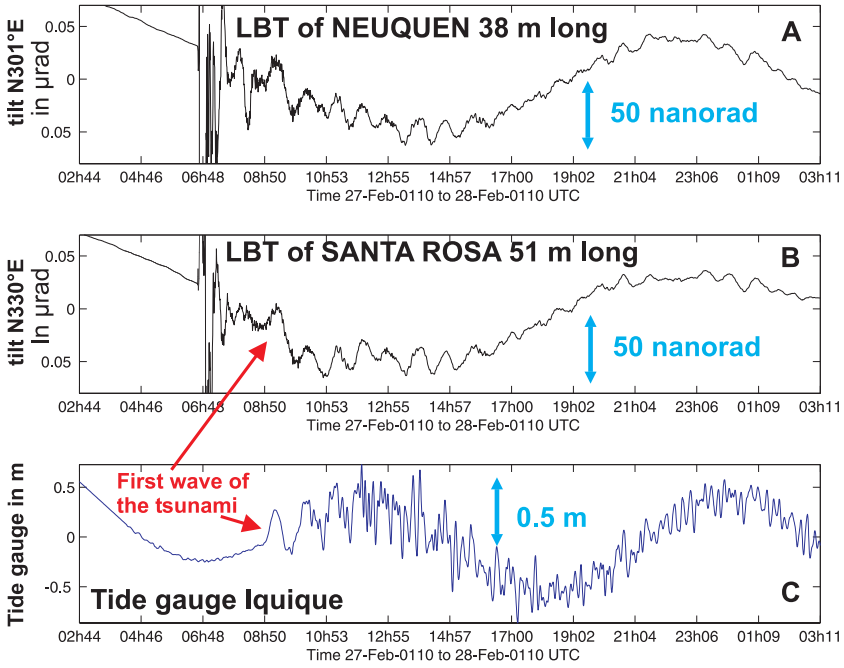

Figure 6. Comparison of 24 hr of tilt and sea level for the Maule 2010 event. (a) N301°E tilt observed at the Neuquen LBT. (b) N330°E tilt at the Santa Rosa LBT. (c) Sea level at the Iquique tidal gauge. The first tsunami wave indicated with a red arrow in (c) has a clear signature on the tilt (red arrow in b).

seismometers, such as STS2 or STS1 (Yuan *et al.* 2005; Nawa *et al.* 2007). The tilt is related to the apparent horizontal acceleration a in the same direction by

$$tilt_{\text{obs}} = \sin^{-1}\left(\frac{a}{g}\right), \tag{1}$$

where

$$a = \frac{dv}{dt}. \tag{2}$$

The frequency band of interest for the Maule tsunami (around 1 hr period) is lower than the lowest corner frequency of the transfer

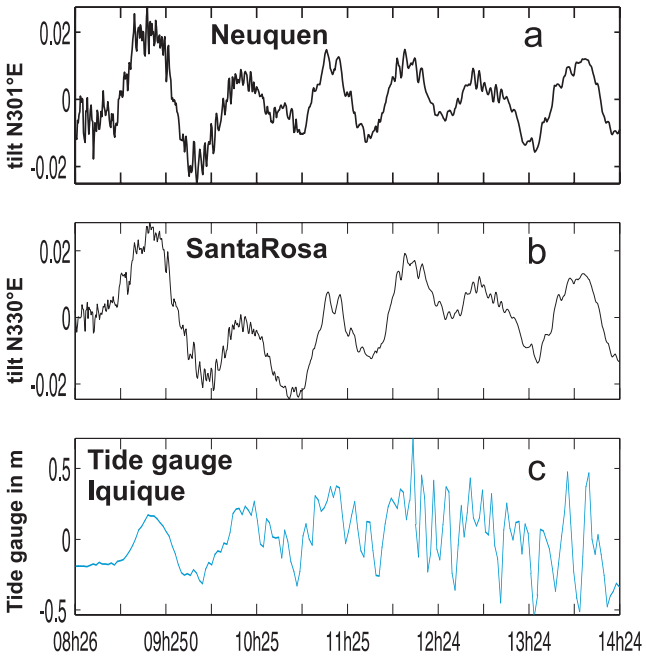

Figure 7. Comparison of 6 hr of tilt and sea level for the Maule 2010 event. Zoom of 6 hr of the signals of Fig. 6: (a) N301°E tilt at the Neuquen LBT. (b) N330°E tilt at the Santa Rosa LBT. (c) Sea level at the Iquique tidal gauge.

function (120 s period for an STS2). Thus, there is a strong phase shift as well as amplitude reduction (90 per cent) of the ground acceleration, which must be deconvolved by the transfer function.

We present in Fig. 8, the broadband horizontal accelerations at the HMB station, close to the tiltmeters (22.5 km) and to the Iquique tide gauge (28 km). We know that the mean gravity near the IPOC network is $g = 9.787\ \mathrm{m\,s^{-2}}$ (S. Bonvalot, personal communication). The acceleration is expressed in terms of tilt, 1 μrad corresponding to $9.787\ \mu\mathrm{m\,s^{-2}}$, from (1). The records in Figs 8(c), (d) and (e) are bandpass filtered with a Butterworth filter of order (zero-phase acausal) 2 between 800 s (1.25 mHz) and 3 hr, showing a clear long-period signal on both NS and EW components, very similar to the sea level record at Iquique; the discrepancies at smaller periods between sea level and tilt records will be discussed later.

5 MODELLING OF THE 2010 MAULE TSUNAMI IN NORTHERN CHILE

Because the tsunami-induced tilt signal depends on load sources (sea level) distributed over a large area, it cannot be expected to be exactly in phase with the local tide gauge record. The joint interpretation of the tidal and the tilt signals related to the tsunami wave is thus not straightforward, and requires, as a first step, an adequate modelling of the tsunami wave.

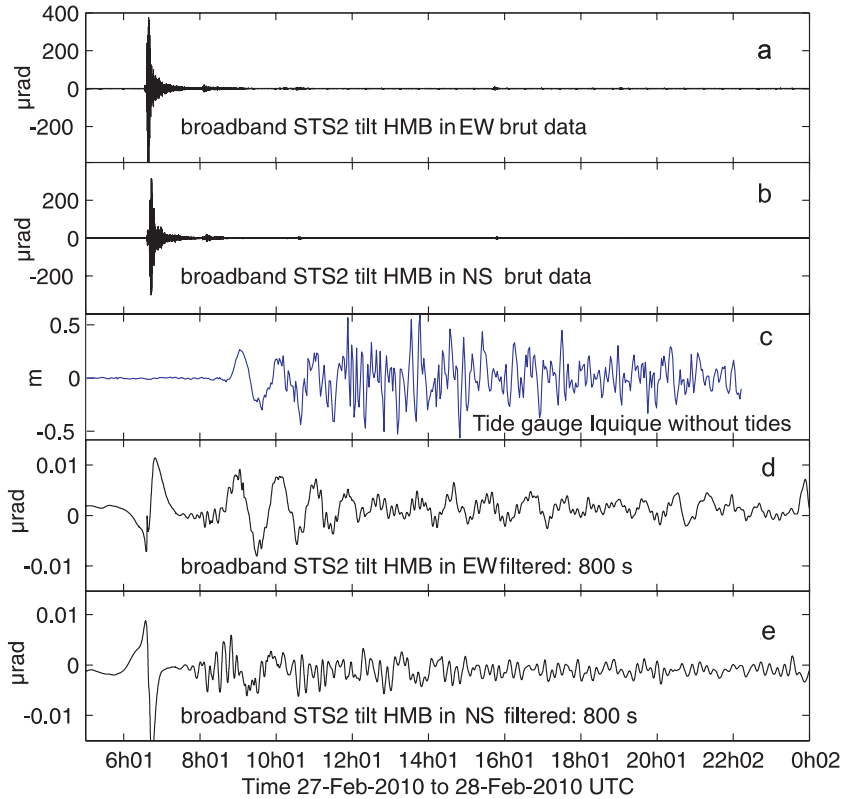

Figure 8. Comparison of 18 hr of tilt (STS2 and LBT) and sea level for the 2010 Maule earthquake. (a) Equivalent tilt in the N180° direction at HMB. (b) Equivalent tilt in the N270°E direction at HMB. (c) Tidal gauge at Iquique. (d) Equivalent tilt in the N180° direction at HMB, bandpass filtered from 800 s to 3 hr. (e) Equivalent tilt in the N270°E direction at HMB, bandpass filtered from 800 s to 3 hr. Tilt is calculated from the horizontal acceleration after deconvolution from instrumental response. The filtered tilt at HMB clearly shows an oceanic signature, as well as seismic noise.

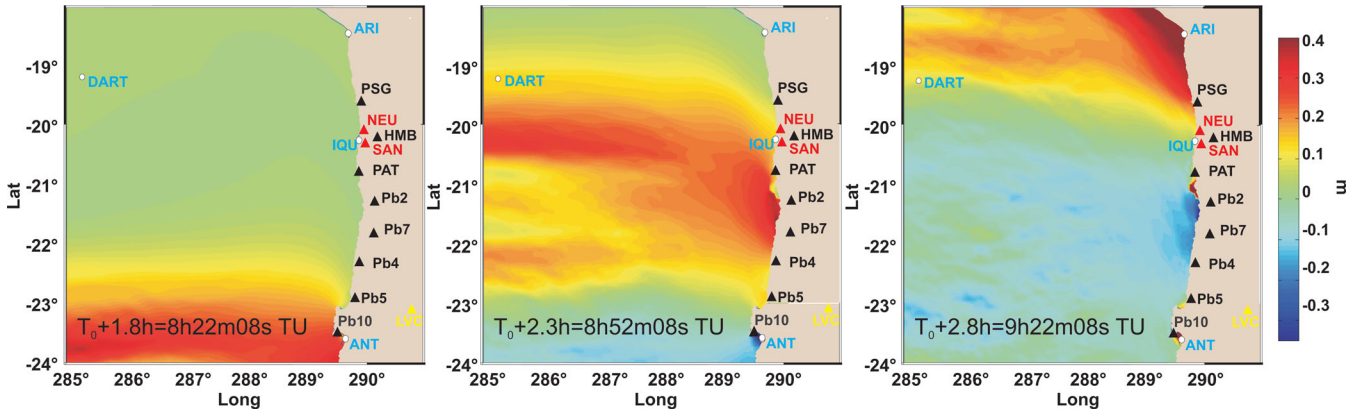

Figure 9. Modelling of tsunami propagation for the 2010 Maule earthquake along the northern Chile coast. Snapshots of the sea level shown at three successive times ($To + 1.8$ hr, $To + 2.3$ hr, $To + 2.6$ hr), where To is the origin time of the earthquake. The times were chosen close to the arrival time of first maximum at Antofagasta, (left), Iquique (centre) and Arica (right).

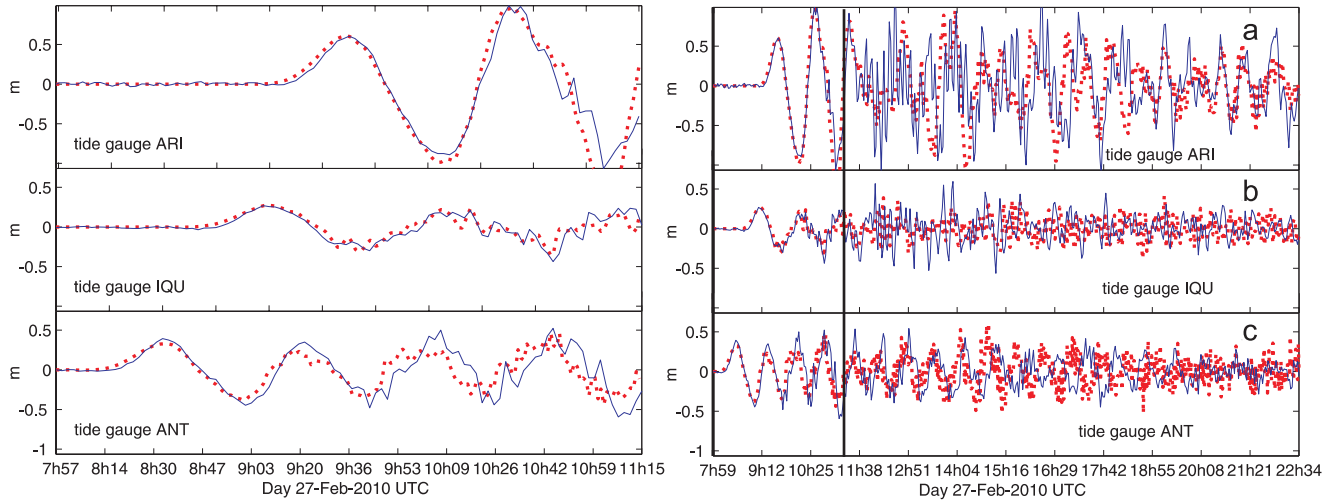

Figure 10. Tsunami records on three tide gauges for the 2010 Maule earthquake. Data (solid blue line) and synthetic (dotted red line) observed at the tidal gauges at Arica (a), Iquique (b) and Antofagasta (c). (Right) 15 hr of record; the vertical bar indicates the time segment shown on the left. The zoom shows the first 3 hr of tsunami.

The oceanic gravity wave propagation is modelled by using a finite-difference numerical scheme (Hébert *et al.* 2001), which solves the shallow water equations in the long-wave approximation. The speed of the tsunami can be approximated by the relation $c = (gh)^{\frac{1}{2}}$. The computation was performed using the high-resolution bathymetric grid GEBCO (IOC *et al.* 2003) (grid size 30″, approximately 900 m), between Lat. 17°S and 26°S and Lon. 70°W and 78°W (or approximately 1000 × 800 km). The seismic source parameters of the Maule event are taken from the inversion results of Delouis *et al.* (2010) to generate the initial water height distribution of the tsunami. We use a sampling rate of 1 min to be consistent with the LBT records and the tide gauges of Arica, Iquique and Antofagasta. A snapshot of the sea level at three different times during the course of the tsunami propagation is plotted in Fig. 9. We compare the predictions of this tsunami model with the observations of the three tide gauges. In the modelling, the tide gauges are located close the shore line, within the resolution of the grid (about 600 m offshore). The predicted sea level at the three sites shows a very good fit to the data, in amplitude and phase, particularly for the first hours (10 per cent error misfit in amplitude and 1–2 min error in delay), as shown in Figs 10 and 11. We checked that the sea level prediction is correct for all the tidal gauges from Valparaiso to Arica. Note that we made no *a posteriori* adjustments of the model, neither of the seismic source location and timing, nor of the bathymetry. A good fit to the coastal records proves that the bathymetry that we used was correct, and insures a correct prediction of the near-coastal sea level change which will dominate the tilt. Note that the closest offshore tide gage (DART), located 500 km to the west at the latitude of Arica (see Fig. 1), will be of great importance for constraining these models for future large tsunamis.

6 MODELLING OF THE DISPLACEMENT, TILT AND GRAVITY EFFECT FROM THE OCEANIC LOAD

The next step is to calculate the effects of the tsunami load on displacement, tilt and gravity change at various on-land recording sites (STS2 and LBTs). The numerical modelling of the tsunami produces a map of sea level change every minute. We consider three main effects of the sea level perturbation on the horizontal acceleration (apparent tilt): (1) an elastic tilt due to the load; (2) a gravitational attraction by the mass of water; (3) an inertial

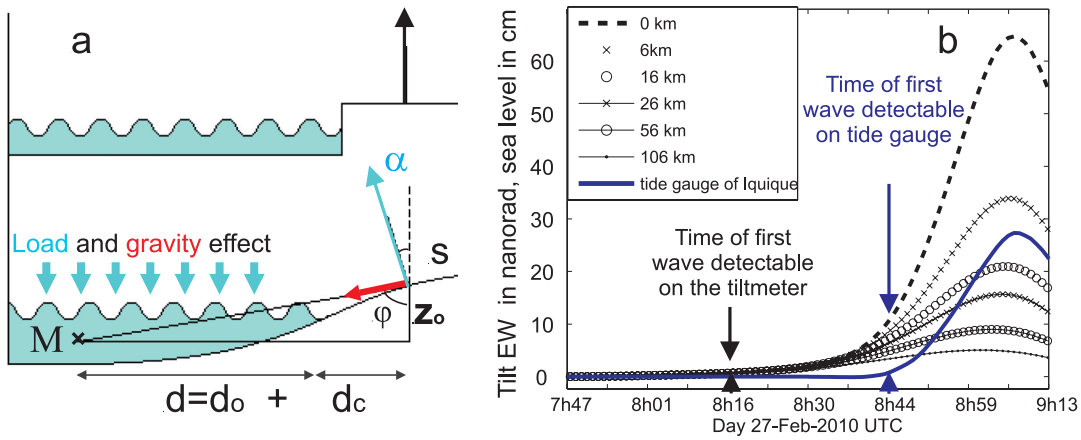

Figure 11. (a) Schematic description of load and gravity effect produced by the tsunami. The true tilt (rotation α of the vertical, blue arrow) produces a horizontal component of the Earth gravity and the gravitational attraction of the water mass (red arrow) produces another contribution to the horizontal acceleration. d_c is the distance from the station to the coastline. d_o, the distance between the coast and the mass of water element. φ is the declination of the gravitational attraction of this element. z_o is the altitude of the station relative to the sea level. (b) Modelled tilt at the latitude of Neuquen for the 2010 Maule earthquake. Time evolution of the EW tilt for different distances of the site to the coastline (d_c) shown at the latitude of the Neuquen tilt site. Black arrow indicates the time of first detectable tsunami-induced signal on tilt. Blue arrow indicates the time of first detectable sea wave on tide gauge.

horizontal acceleration due to elastic displacement of the site. Note that these signals are not separable in the tilt record.

Considering first the elastic tilt for each sea level map, we computed the static strain produced by this surface pressure following an adaptation of the Boussinesq problem (point source at the surface of an elastic half space) for a more realistic earth structure (Farrell 1972; Pagiatakis 1990). For this, we consider the Green functions for a spherical, radially stratified earth model, provided by Pagiatakis (1990). The Green's functions depend only on the angular distance between the vertical point force load and the station, and are calculated using tabulated load Love numbers. The resultant tilt (Fig. 11a) due to a set of n pressure loads due to masses M_i ($i = 1, n$) applied to the n element of the grid is

$$tilt_{\,\mathrm{mod}} = \sum_{i=1}^{n} \frac{Ct_i(r_i) \cdot M_i}{r_i^2}, \tag{3}$$

where $Ct_i(r_i)$ are the Green's functions and r_i is the angular distance between the tilt measurement site and the load point. Similar expressions hold for the vertical and horizontal displacement at the sites:

$$dispV = \sum_{i=1}^{n} \frac{Cv_i(r_i) \cdot M_i}{r_i} \tag{4}$$

and

$$dispH = \sum_{i=1}^{n} \frac{Ch_i(r_i) \cdot M_i}{r_i}, \tag{5}$$

where $Cv_i(r)$ and $Ch_i(r)$ are the Green's functions for the vertical and horizontal displacement, respectively (Pagiatakis 1990). These displacements, for the period T of the tsunami, produce vertical and horizontal inertial accelerations equal to $-(2\pi/T)^2$ *dispV* and to $-(2\pi/T)^2$ *dispH*, respectively. The horizontal inertial acceleration remains small with respect to the gravitational attraction, and can thus be neglected. In Appendix A, we show that the inertial horizontal acceleration is approximately 1000 times weaker than the acceleration produced by the load effect.

The excess of water mass near the ocean surface at each grid point, M_i, leads to a perturbation of the gravity which is equivalent to a horizontal acceleration (Fig. 11a). The latter can be written according to Newton's law:

$$gravity_i = \frac{G \cdot M_i}{r_i^2} \sin\varphi, \tag{6}$$

where $\boldsymbol{G}$ is the universal gravity constant, r_i the distance between the station and φ is the declination.

Nearly 20 broadband stations of the IPOC network between Arica and Antofagasta were available. However, not all were used in the present study, due to the rapid decay of the tilt with distance. This decay is illustrated in Fig. 11(b) where we plot the synthetic tilts calculated at increasing distances d_c from the coast. Interestingly, the installation of a few of the IPOC STS2 sites very close to the coast was precisely aimed at a better detection of tsunamis.

7 COMPARISON OF TILT DATA AND MODEL FOR THE 2010 MAULE TSUNAMI

We modelled the records of 10 broadband stations in addition to those of the LBTs. We applied a zero-phase acausal bandpass filter between 800 s (1.25 mHz) and 3 hr, on all the data, to remove the seismic waves which mask the early phase of the tsunami. Synthetics were also filtered in the same way.

We first present the result for the Neuquen and Santa Rosa LBTs stations, 7 and 9 km from the coastline, respectively (see Fig. 1). As shown in Fig. 12, the synthetic tsunami-induced tilt (dotted, red curves) has a very small amplitude, 45 nrad peak-to-peak at Neuquen and 35 nrad at Santa Rosa (equivalent to a relative vertical displacement of about 0.4 mm on a base of 10 km). These synthetics are very similar to the recorded signals (black, solid curve in Fig. 12) with less than 10 per cent misfit in amplitude and phase for the first two or three oscillations. Larger differences in phase appear after a few hours, due to difficulties in accurately modelling the resonance effects between the coast and the trench, but the spectral amplitude and the dominant period remain correctly modelled.

The results for the IPOC STS2 stations are presented in Figs 13 and 14, where we compare the observations (black solid line) to the synthetics (red dotted lines). Generally, the modelling of the first tsunami-induced tilt oscillation presents a good correlation with the

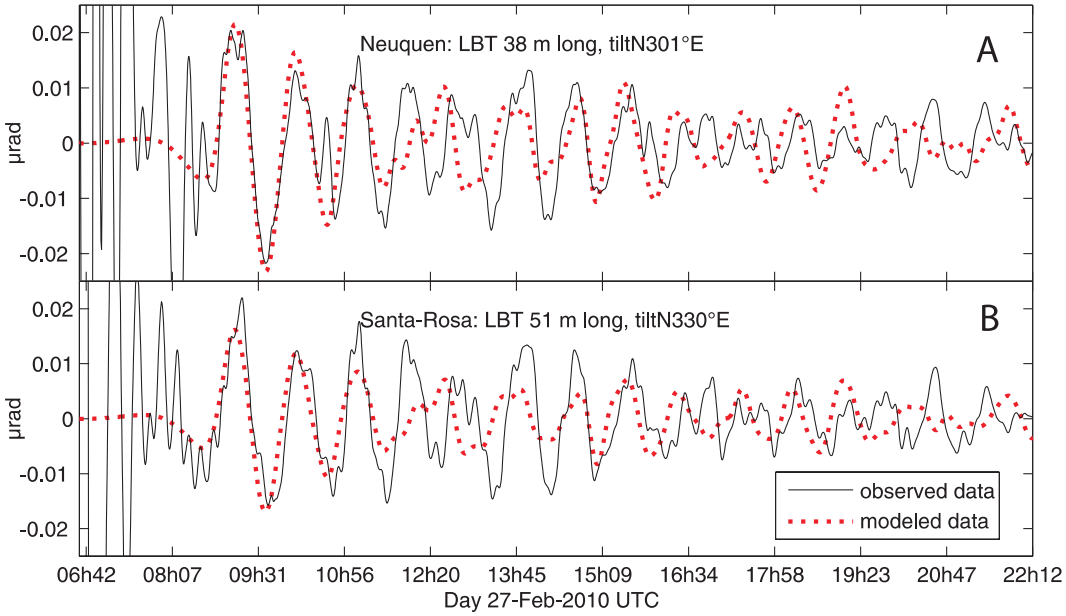

Figure 12. Comparison of recorded and modelled tilt at Neuquen and Santa Rosa for the Maule 2010 earthquake. Observed (solid black) and modelled (red dotted line), bandpass filtered from 800 s to 3 hr for the LBTs at Neuquen (a) and Santa Rosa (b). The model is calculated from the ocean load and the gravitational attraction of the displaced water mass. The tsunami has a well-resolved modelled tilt signature of about 40 nrad, correctly modelled during the first 3 hr.

acceleration records. The fit is particularly good for both EW and NS components at stations PSG, HMB, PB05 and PB07, which are not too close to the coast (between 7 and 20 km). The maximum relative errors of about 10 per cent are similar to those obtained on the LBTs. Larger misfits can appear for the stations closest to the coast (1–3 km), such as PAT (Fig. 13) and PB10 (Fig. 14), with a difference in the first wave amplitude which can reach 50 per cent, or with phase shifts affecting only one component (e.g. NS component of PAT).

For PAT, the modelling of the EW component of the first wave is in good agreement with the observation, while that of the NS component is delayed by about 20 min with respect to the observation. This station, which is very close to the coast, is expected to be sensitive to very local variations of water level, which may not be properly modelled with our coarse bathymetric grid. More specifically, the late arrival of the NS tilt in the model can be explained by a late modelling of the sea level rise near the shore line just south of PAT (which controls the early NS tilt), associated with a correct modelling of the offshore propagation (which controls the early EW tilt). This is well illustrated in Fig. 15(a), at a time where the modelled tsunami has reached the latitude of PAT far offshore, but has not yet reached the shallow waters south of PAT, close to the coast, due to the strong reduction in the velocity of the gravity waves. A refined, improved bathymetry—and possibly source model—is therefore requested for a better modelling of these very local effects.

More to the south, the PB10 station is very close to the Antofagasta bay and detects a strong resonance at about 43.4 min period (Figs 14g and h). This period is very similar to that recorded during the 2007 Tocopilla Event, 50 km to the north of Antofagasta. The tilt measurement can thus provide accurate information on the tsunami wave resonance along the coast (Yamazaki & Cheung 2011). As for PAT, the larger misfit at station PB04 (30 per cent) might be related to inaccurate modelling of the tsunami at this latitude.

For stations deep inland such as PSG, HMB, PB07 and PB05 (more than 15 km away from the sea), the effect of near-coastal effects becomes negligible and the tilt is controlled by the well-modelled long wavelengths of the tsunami (see black arrows in Fig. 15a).

The first 2 hr of the tilt direction, plotted in a stereoscopic view in Fig. 15b, show an elliptical pattern, mainly oriented WSW-ENE. The tilt polarization of the first 20 min at PSG and HMB is more towards S-SW, compatible with a positive oceanic load propagating from the south. This early rotation is, however, not apparent at PAT, this may be due to its proximity to the coast and its sensitivity to near-shore complexity of the water level. We remark that although the bulk of the tsunami propagation is towards North (Fig. 15a), the dominant average tilt does not point perpendicular to it (i.e. EW) as would be expected from a simple 1-D propagation. The slight but persistent tilt towards SSW, even for later arrivals (see Fig. 15b), can be explained by a reduction of the tsunami amplitude and its dilution towards west in the ocean, during its northward propagation, reducing the effect of the ocean loads located more to the north. Thus, these observations do not corroborate the assertion by Yuan *et al.* (2005) and Nawa *et al.* (2007) that the maximum tilt is directed in the orthogonal direction to the coast, probably because these authors used stations located very close to the coast (a few hundred metres to a few kilometres).

8 DECAY OF TILT SIGNAL WITH DISTANCE TO THE COAST

The records of the three broadband stations nearest to Iquique, PAT, PSG and HMB (Fig. 13) show that the tilt amplitudes decrease with the distance to the coast, with amplitude varying by a factor of 3–4 between 3 and 26 km, thus consistent with a tilt loading source offshore. The GEOFON LVC station, equipped with an STS1 seismometer, is the most distant, located at about 137 km from the coast. It does not show any low-frequency signals around 1 hr period (Fig. 13), which is consistent with our

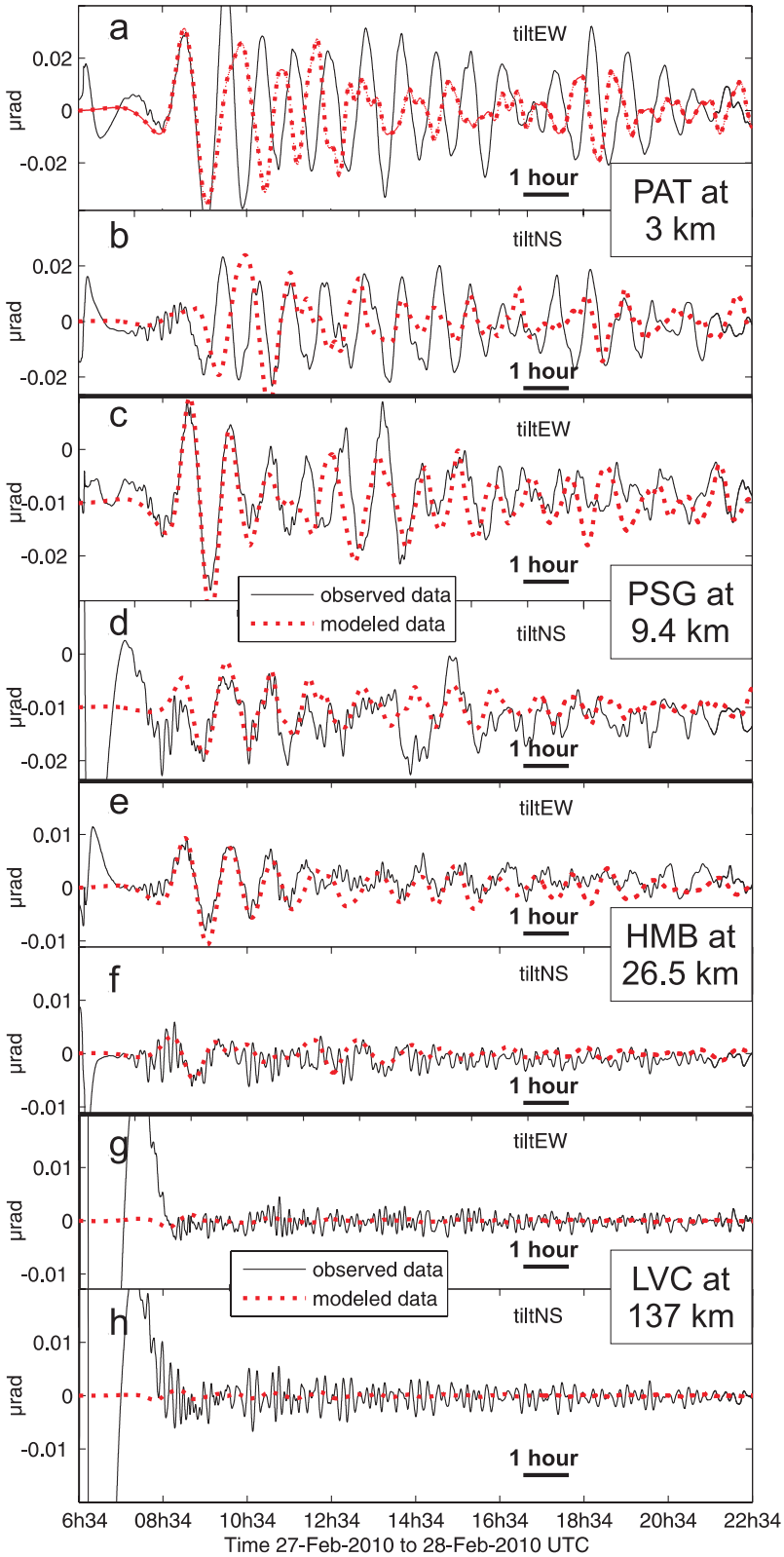

Figure 13. Comparison of recorded and modelled tilt at the STS2 (IPOC/CNRS) sites for the Maule 2010 earthquake. We plot 16 hr of observed (solid black) and modelled (red dotted line), for the EW and NS components of the STS2 from the IPOC/CNRS sub-array and of the STS1 from LVC (GEOFON array) (reference site far away from the coast). Data have been deconvolved from instrument response and filtered between bandpass filtered from 800 s to 3 hr. The model is calculated from the ocean load and the gravitational attraction of the displaced water mass. The distance to the coast is indicated below the name of each station. The tsunami has a well-resolved modelled tilt signature of about 10 to 60 nrad p.p., correctly modelled for the first hours (except for PAT, which is closest to the coast). It is at the noise level for LVC.

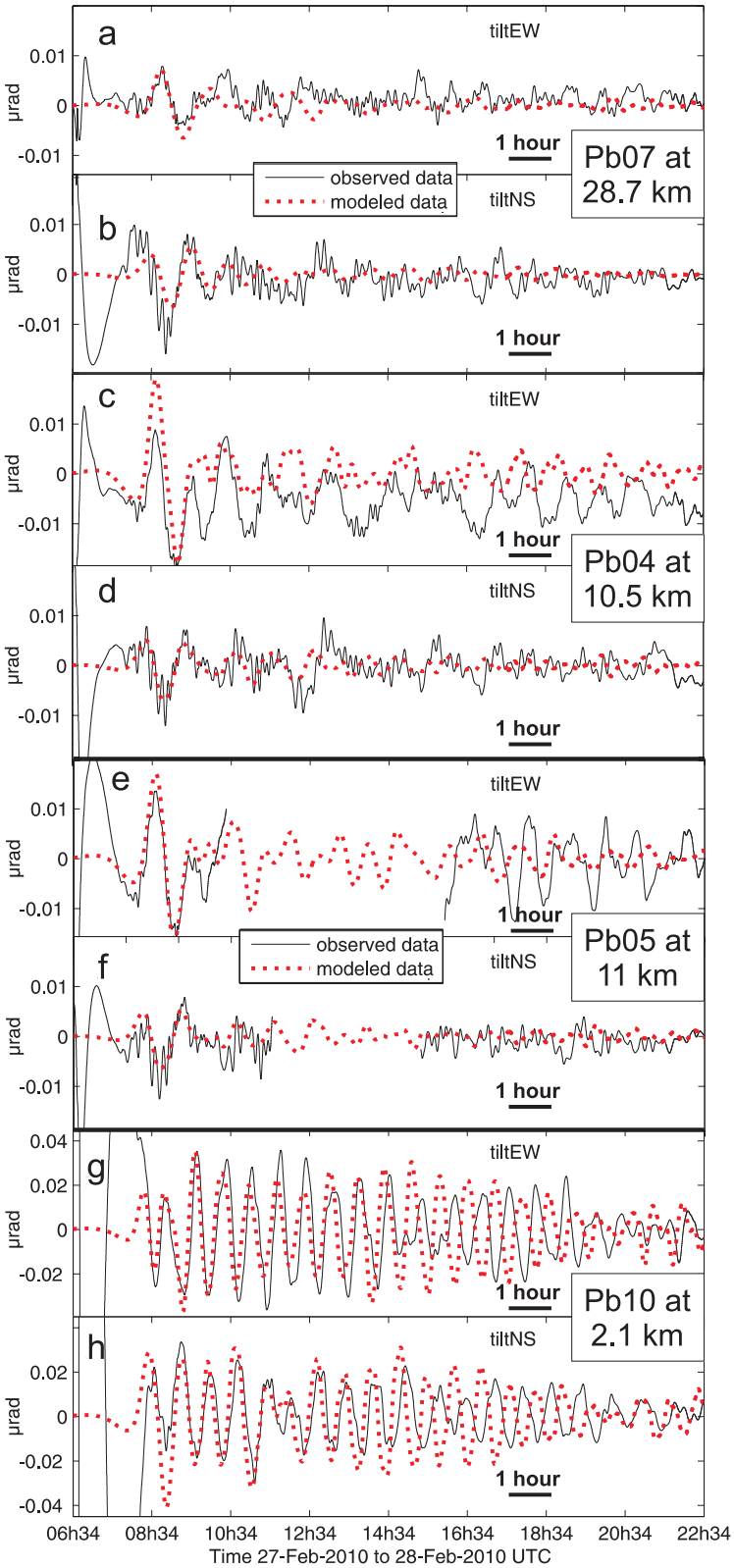

Figure 14. Comparison of recorded and modelled tilt at the STS2 (IPOC/GFZ) sites for the 2010 Maule earthquake. Same legend as Fig. 13, for the STS2 stations of the IPOC/GFZ subarray.

interpretation of a tsunami-induced signal at the other sites, much closer to the sea. LVC can thus be considered as a reference station, unperturbed by the tsunami-induced tilt: therefore, the long-lasting, shorter period signals at LVC (dominant period 600 s) must be of seismic origin. This is confirmed by the fact that they are very similar, in amplitude and phase, to the signals recorded at the other seismic stations of the IPOC array, as shown in more detail in Appendix B.

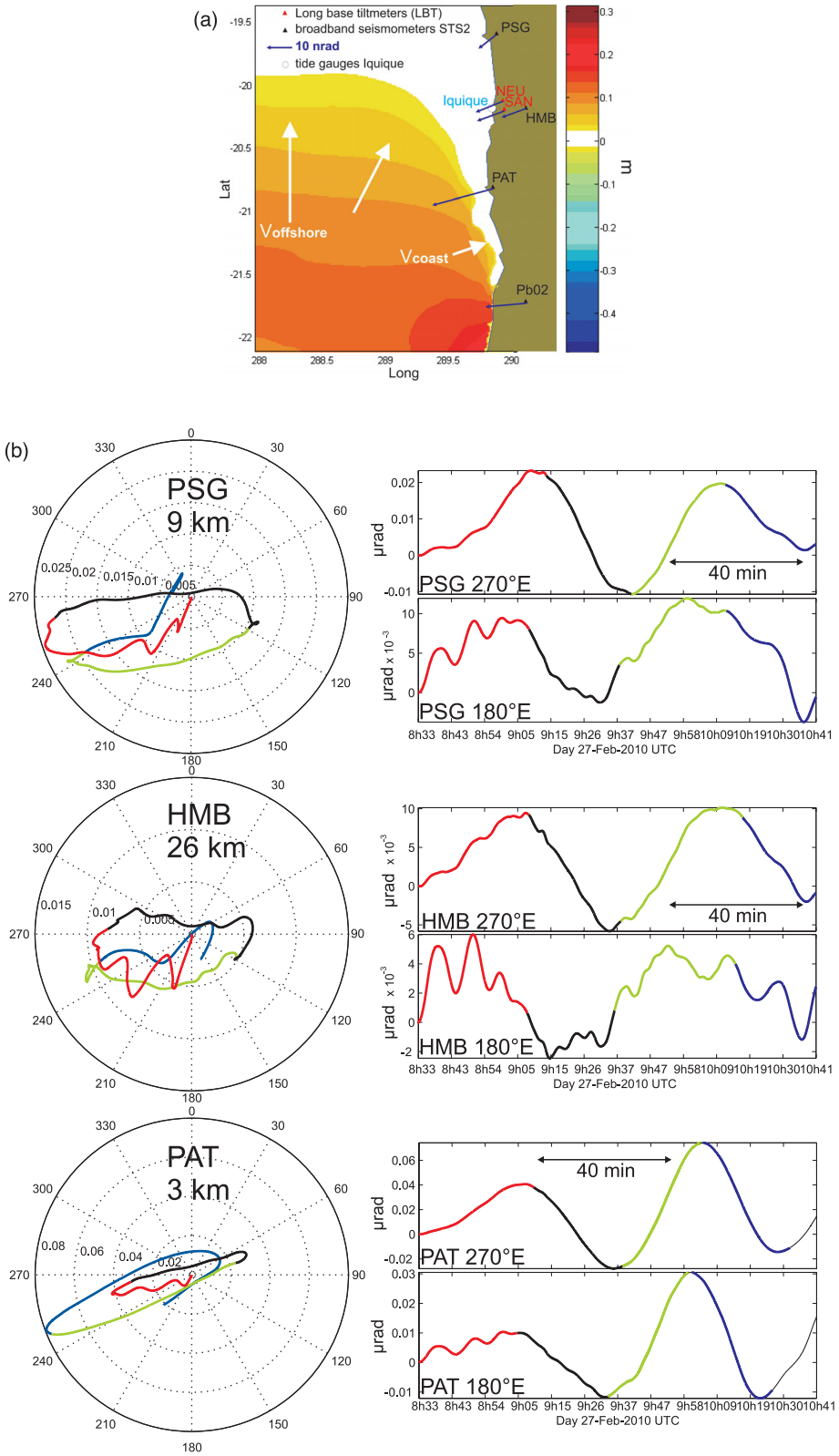

Figure 15. (a) Tsunami heights and polarization near Iquique for the 2010 Maule earthquake. Sea level 20 min before the first maximum is recorded at the Iquique tide gauge (colour code in metres). White arrows represent local direction of wave propagation (arbitrary scale). Blue arrows represent the corresponding tilt direction and amplitude (scale top left) at the stations on the map (red triangles for LBT, black triangles for STS2, white circle for Iquique tide gauge). Note the faster propagation offshore due to the deeper bathymetry, and the complexity—possibly poorly modelled—of the wave front very close to the coastline. We remark the progressive anticlockwise rotation of the tilt direction towards the north; this translates into a clockwise rotation in time of the tilt direction for a given site when the tsunami propagates to the north. (b) Tilt recorded tilt for near-coastal IPOC stations (PSG, HMB and PAT) during the 2010 Maule earthquake. (Left) Stereoscopic plot of tilt polarization at each station; (right) corresponding horizontal EW and NS components of tilt.

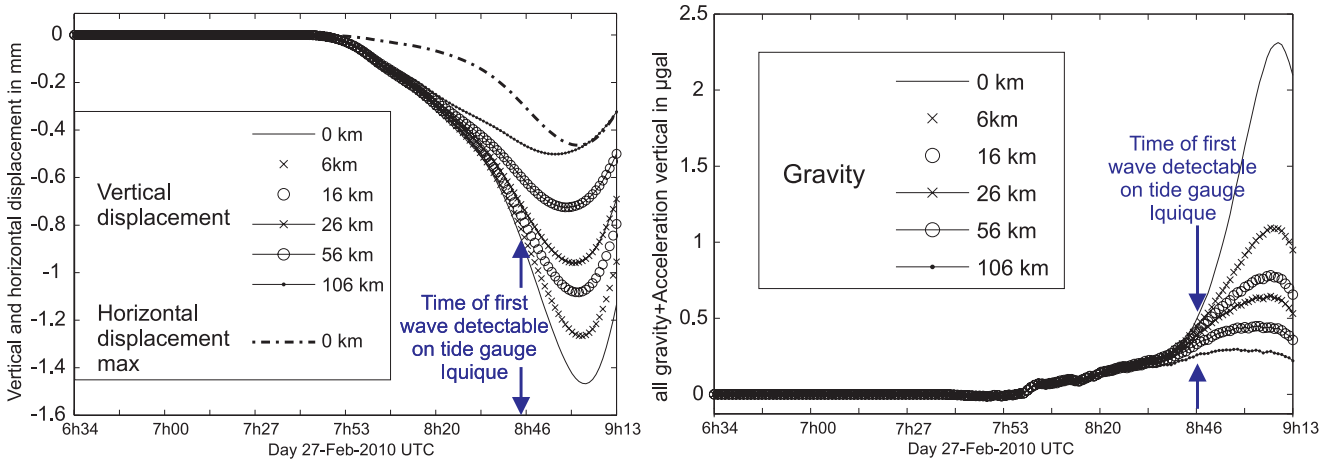

Figure 16. Modelling of the displacements and vertical gravity change for the Maule 2010 earthquake. Time plot (2.5 hr) of the calculated early phase of the tsunami signature on horizontal and vertical displacement (left) and on the vertical acceleration (right). The calculation is done at the latitude of Iquique, for various distances to the coastline (see inset). Arrows show the time of detection of the sea wave at the Iquique tide gauge. The vertical acceleration signal includes all terms of gravity perturbation (see text).

This effect explains part of the discrepancies observed between the tidal records and the tilt records (STS2 and LBTs) reported above (Figs 6 and 8).

9 DETECTABILITY OF THE MAULE TSUNAMI ON THE VERTICAL ACCELERATION OR ON THE DISPLACEMENT

We presented above the clear detection and correct modelling of the tsunami-induced horizontal acceleration. We now investigate the possibility of detecting the tsunami on the vertical acceleration of broadband seismometers or gravimeters. We also investigate the horizontal and vertical components of cGPS.

To model the vertical component of gravity, we introduce: (1) the direct gravitational vertical effect, which is mainly horizontal (Fig. 11a), (2) the change in earth gravity due to the vertical displacement (Fig. 16, left), which is the dominant effect, (3) the inertial vertical acceleration and (4) the effect of the density variation in the Earth. The resulting effect in vertical acceleration is plotted versus time (Fig. 16, right), at the latitude of PAT, for various distances from the coast. It shows a rapid decay of the signal with this distance.

For comparison with data, we select the favourable case of PAT the seismometer situated nearest to the coast. Fig. 17, left, shows the recorded vertical acceleration component (solid black line) and the modelled one (dotted red line). Despite the large seismic noise, there is a weak but significant correlation between data and synthetics, in phase, with predicted amplitude slightly smaller than the recorded one. The synthetic gravity signal reaches 0.5–1 µgal, which would be barely detectable with an absolute gravimeter FG5 or A10, which has a resolution of 1 µgal. Superconducting gravimeters, with a resolution of some nanogals, would enable its detection.

The difficulty for detection also arises from the large noise amplitude on the vertical component. The analysis of the vertical signal at LVC, far from the coast, thus unperturbed by the tsunami effects,

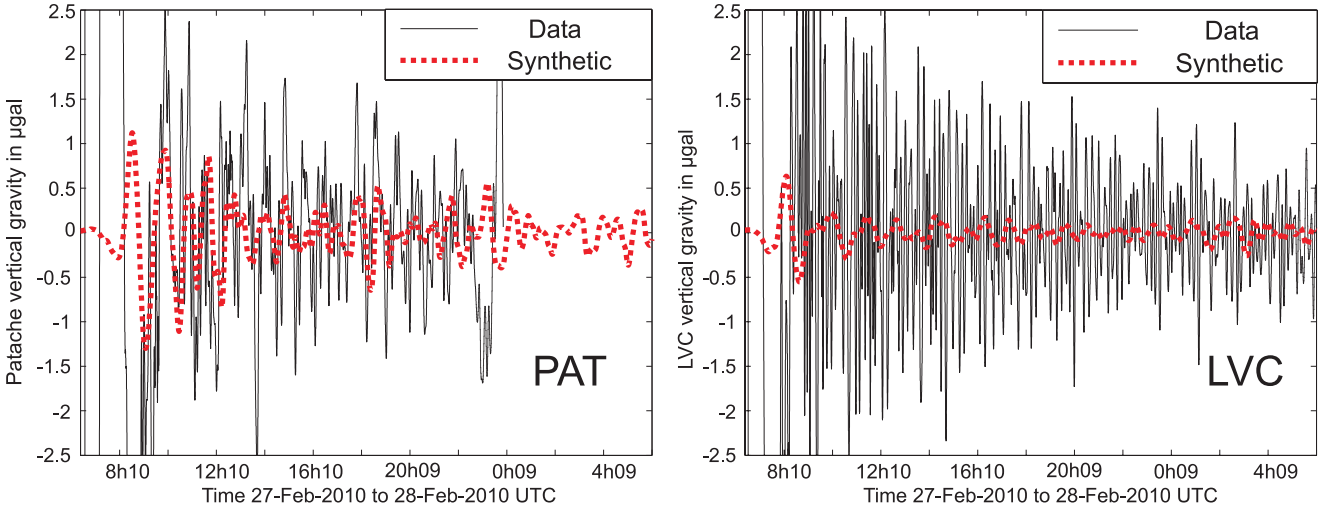

Figure 17. Modelled and observed vertical acceleration at PAT and LVC during the 2010 Maule earthquake. (Left) PAT vertical acceleration. (Right) LVC vertical acceleration. Solid black line: data; dotted red line: synthetic. Both records are shown with the same vertical scale, in micro-gals (equivalent gravity changes). All signals are bandpass filtered between 800 s and 3 hr. Both stations present the same level of observation (dominated by seismic waves). The tsunami modelling has a clear effect on both stations, though smaller at LVC due to distance, and both are much smaller than the seismic background noise.

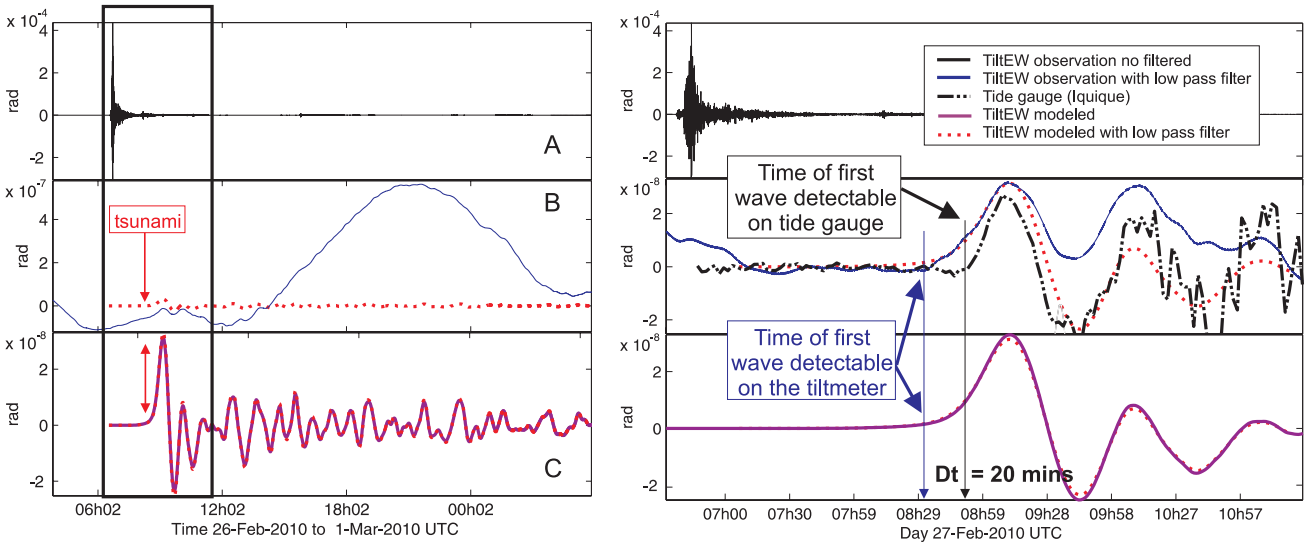

Figure 18. Early phase of STS2 observed and synthetic tilt at PSG for the 2010 Maule earthquake. (Left) 24 hr of signal; (right) zoom on the first 5 hr of signal. (a) EW tilt data computed from horizontal acceleration at PSG; (b) EW tilt at PSG, low pass filtered at 800 s (elliptic filter order 3), solid blue line shows the data, dotted red line is the synthetic computed from the tsunami model with the same filter; (c) synthetic EW tilt (same as red dotted line in (b), with enlarged vertical scale), unfiltered (solid purple line) and filtered (dotted red line) with the same filter as in (b). The rectangle in the figure to the left indicates the frame of the zoom on the right. Red and blue arrows point to the first signature of tsunami on tilt. Black arrow (right) points to the arrival time of tsunami on tide gauge (thin vertical black line).

shows the same noise level, in the 800 s to 3 hr period range, which is then clearly identified as seismic noise dominated by normal modes. A last difficulty is the instability of gravimeters during strong shaking producing spurious jumps in the data which can contaminate later signal when low-pass filtered.

The vertical displacement on the coastline is modelled in Fig. 16(a). It reaches a maximum value of 1.5 mm, which is barely above the noise level of the best processed GPS records and hence is not detectable by this type of instruments. We remark that the horizontal displacement is typically three times smaller, ∼0.5 mm (see Fig. A1, left), so that the GPS record would not resolve the horizontal motion either, at this level of amplitude (Elosegui *et al.* 2006). Elosegui found that the root-mean-square error of the 1-Hz GPS position estimates over the 15-min duration of the simulated seismic event was 2.5 mm, with approximately 96 per cent of the observations in error by less than 5 mm.

Thus, one can infer from this modelling that tsunami amplitudes five times larger than what is observed for Maule, typically about 2 m, would be at the limit of theoretical detection on coastal GPS and near-coastal gravimeters.

10 DETECTABILITY AND MODELLING OF THE EARLY PHASE OF THE TSUNAMI-INDUCED TILT

We demonstrated above, on the Maule records, that one could accurately model the recorded horizontal acceleration and tilt load signal of tsunami water masses. In particular, from the eqs (3) and (6), it can be shown that water loads located hundreds of kilometres away can produce a detectable tilt signal. For example, a sea level rise of 50 cm uniformly distributed on a rectangular surface of 100 km (EW) by 500 km (NS), with its closest edge being located 100 km W from the coast, produces a tilt larger than 10^{-8} rad at the coast. The resolution and stability of the tilt and seismometer stations being equivalent to 10^{-9} rad at periods up to several hours, one should observe the load effect before the related tsunami waves reach the coast close to the monitoring site.

The main difficulty comes from the disturbing effect of the seismic waves generated by the seismic rupture. As an example, on the broadband station of Pisagua, the amplitude of the unfiltered seismic acceleration record is 1000 times larger than the amplitude of the tsunami signal (zooms in Figs 18a and b). However, on the unfiltered LBT records, the seismic noise is five times weaker than the signal resulting from the tsunami (see Figs 6a and b), because the long water tube acts as a low-pass mechanical filter (Boudin *et al.* 2008).

Other sources of difficulties for identifying the tsunami are the various low-frequency signals due to Earth tides, barometric pressure and temperature. The earth tides can be quite accurately predicted, or, being periodic, simply adjusted (in the present study, we use the ETERNA3.3 software, Wenzel 1996). The thermal and pressure effects are more difficult to model, as the transfer functions may have frequency dependence, but they are expected to have dominant periods of a few hours or more, outside the range relevant for tsunamis.

In all the cases, the LBT is more stable and less sensitive to the local perturbations described above than the short-base instruments—including the STS2 (Agnew 1986; Boudin *et al.* 2008; Longuevergne *et al.* 2009). This can be checked at the time of the tsunami of Tocopilla (Fig. 5 and part 3).

In order to reduce these low-frequency perturbations, the results presented above (Figs 12–14) use a zero-phase acausal, symmetric bandpass filter between 800 s and 3 hr. But this filter produces small, spurious energy arrival related to the low-frequency cut-off of the filter, which could alter our analysis of the earliest phase of the tsunami signal. To avoid this effect, in the following, we only low-pass filter the signal at 800 s, which suppresses detectable forerunners (an alternative way would be to use causal filtering, which, for the present case, produces the same result as the tsunami energy around 800 s is negligible). We checked on the records that this filter does not affect the low-frequency observations of the tsunami

(Fig. 18c) and, in particular, does not modify the phases of the tilt. We have applied this low-pass filter on the 1 Hz tilt record (blue curve in Fig. 18b) and find that it efficiently removes the seismic noise.

For the LBT, the sampling rate is much smaller, 1 pt/30 s. Although this sampling rate is well adapted to the low-pass filtering effect of the viscous water flow in the tube (characteristic eigenperiod of a few minutes), it is not able to filter out the various liquid and solid resonance effects, at frequencies of a few to several Hz, of the measuring vessels at both ends of the water tube, which results in aliasing effects with spurious long-period signals, especially during seismic shaking. A sampling rate of 100 Hz, on trigger during the many hours of the seismic and tsunami event, would allow a more efficient filtering without aliasing effects.

Another problem arises when high-pass filtering, due to the spurious phase appearing at the time of the main seismic waves (see, e.g. Figs 8d and 9e). All broadband stations show the same spurious signal after filtering, except the EW component at Pisagua (see Fig. 13c). We believe that this is due to a step or ramp within the seismic signal, caused by a mechanical instability of the seismometer at the contact point to the ground, or on the surface rock layer. Thus, such effects might be avoided or reduced during the installation phase by the selection of stable, unfractured bedrock and the careful coupling of the instrument to it.

To avoid the difficulty above, we have worked on the unperturbed EW Pisagua component. The signal corrected from earth tides is plotted in Fig. 18b, right (solid line). We can compare it to the model calculated from the tsunami load (red dotted curve) in Fig. 18(b), and find an excellent fit for the first half period (about 30 min) of tsunami signal. For later times, both curves progressively diverge: Although the tsunami component at 1 hr period remains very similar on data and synthetics, a longer period, unmodelled signal appears in the data, possibly due to thermal or pressure effect. We plotted the records of the tide gauge of Iquique harbour (black dotted curve) on the same Fig. 18(b), which clearly shows that the tsunami-induced tilt signal at Pisagua starts about 15 min before the tsunami record at tide gauge, although the latter is located at 70 km to the south of the Pisagua station, *a priori* favouring an earlier detection. One can estimate the additional delay time, for the tsunami propagation, between the latitude of Iquique and that of Pisagua to be of the order of 7–9 min. This leads to an advanced time of 22–24 min for the detection of the tsunami at Pisagua, with respect to the arrival time of the tsunami on the shore line at the latitude of Pisagua. Such an early detection of tsunamis with tilt records could be used to improve tsunami warning systems.

11 TSUNAMI SIMULATION FOR A POSSIBLE MEGATHRUST EARTHQUAKE IN SOUTHERN PERU

One may consider a scenario with a future megathrust earthquake with the same magnitude and location as the 1877 Iquique earthquake (Mw8.8), but its source, along the northern coast of Chile, would be in the immediate proximity of the tilt array. The tsunami would thus arrive at the coast only a few to 10 min after the start of the earthquake, and the tilt signals due to oceanic loading would be covered by the expectedly much larger tilt signals due to the seismic source (long-period waves and near-field terms). The present tilt array would thus not contribute to detect and constrain such a tsunami event.

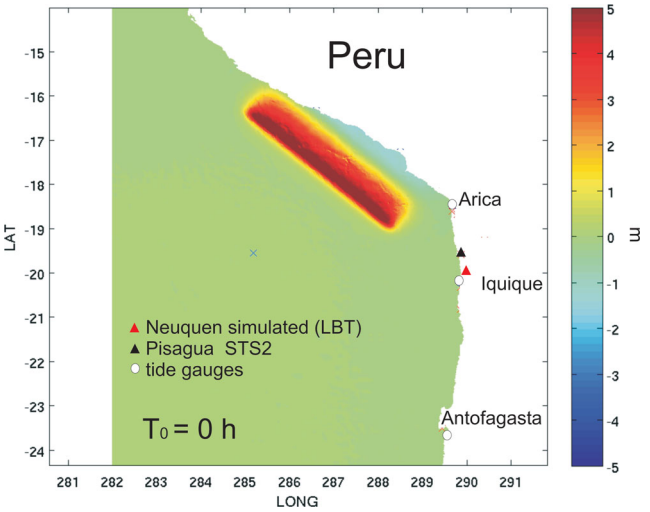

Figure 19. Model of tsunami for a $M = 8.8$ scenario earthquake in southern Peru. Sea level is plotted just after the seismic event (amplitude colour coded, in metres).

But an earthquake source like that of the 1868 southern Peru (Mw8.8) is much further away from the considered Northern chilean array, and the related tsunami might arrival well after the perturbing seismic waves. In order to illustrate further the feasibility to detect this tsunami, we thus assume a plausible seismic source scenario with a magnitude $Mw = 8.8$ earthquake rupturing the interplate contact between Arequipa (Peru) and Arica (Chile) (rectangle in Fig. 19). In this scenario, the seismic source is much closer (400 km) to the instruments than in the case of the 2010 Maule event (1800 km). The slip on the fault is taken identical to that used for the Maule event, and the resulting tsunami is modelled with the same method and using the same bathymetric grid as for Maule. The detection test is achieved at the LBT site of Neuquen, close to Iquique. We selected this site because this instrument, continuously recording at 1 Hz, has the best stability among all the other IPOC sites presented in this paper, with negligible sensitivity to pressure and temperature at periods of minutes to hours, and no expected non-linear behaviour (steps) related to moderate shaking. In order to include a realistic main shock seismic signal to the modelled tilt, we simply scaled the Maule acceleration record at station Pisagua by a factor of 2 (representing a very conservative correction for distance effect) and added it to the tsunami-induced synthetic tilt. The resulting synthetic tilt is plotted in Fig. 20, together with the modelled sea level at Iquique. The first sea wave reaches a maximum of 3.5 m, corresponding to a maximum tilt 0.2 μrad. The main result is that the tilt signal, low-pass filtered at 800 s, is detectable 12 min before the tsunami reaches the coast at the same latitude. This delay is shorter than for the observed Maule tsunami, mostly due to the shorter wavelength of the first upward motion in this scenario.

12 DISCUSSION AND CONCLUSION

In this paper, we have provided new, clear evidence for tsunami-induced tilt, by analysing the records of the LBTs and broadband seismometers of the northern Chile IPOC arrays, for the 2007 Tocopilla and the 2010 Maule earthquakes. We correctly modelled the first hours of the tilt for the Maule tsunami, showing the adequacy of both the tsunami modelling (source and propagation) and of the modelling of the horizontal acceleration due to the ocean-level perturbation. The latter affect the tilt signal in three ways: (1) the

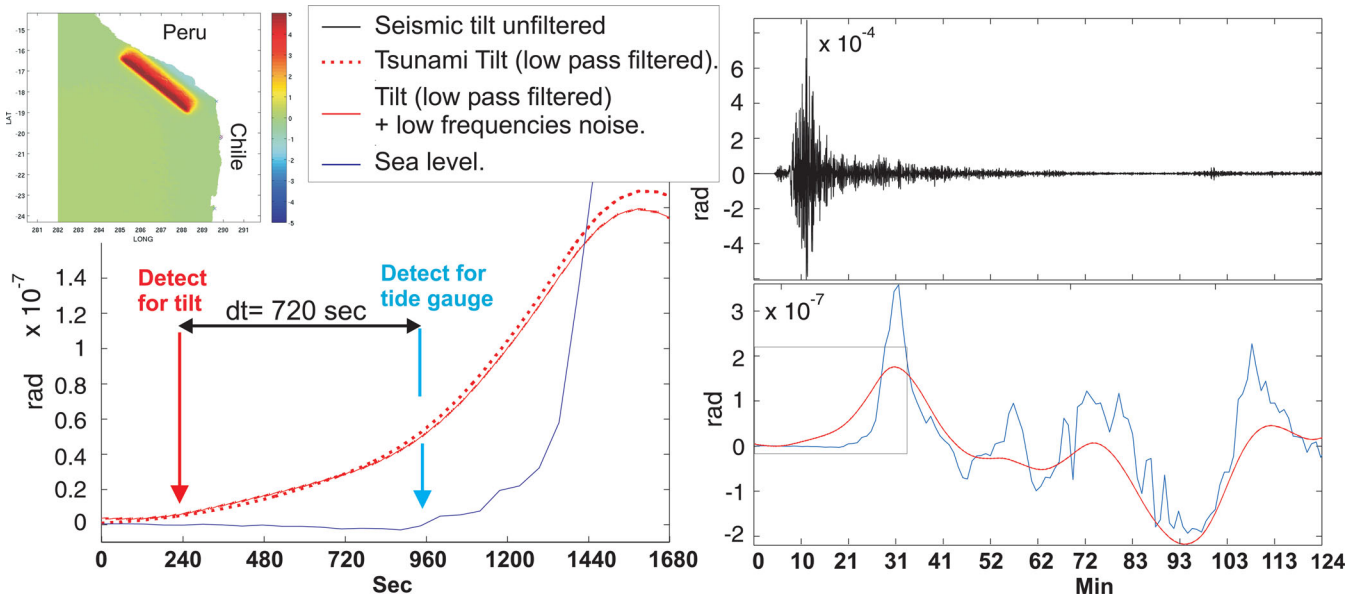

Figure 20. Simulated early phase of tilt and sea level for a mega-thrust event in southern Peru. The tilt is calculated in the EW direction at the Neuquen LBT site, for a tsunami generated by a possible megathrust earthquake in southern Peru ($Mw = 8.8$) (see Fig. 19). (Right) 124 min of signal. (Top right) Synthetic horizontal acceleration simulating the seismic noise from the earthquake. (Bottom right) Red line is for the low-pass filtered EW tilt resulting from the modelled tsunami-induced tilt. Dotted red line shows the sum of the low-frequency pressure, thermal or seismic noise and the modelled tsunami-induced tilt. Blue line is the modelled sea level at the Iquique tide gauge close to Neuquen. (Left) Zoom of the bottom right figure, for 1680 s of signal. Same lines as in bottom right figure. Dotted red line: low-pass filtered tsunami-induced tilt alone (no pressure, thermal or seismic noise added). In this test, the detection time of the tsunami on the tilt records (red arrow) is 720 s earlier than for the tide gauge (blue arrow).

elastic tilt response to surface loading; (2) a horizontal, gravitational attraction by the water mass and (3) an inertial horizontal acceleration. As explained in Appendix A, these effects at the period of 1 hr are in a proportion of approximately 80, 20 and 1 per cent, respectively. At shorter periods, which might be observed for tsunamis generated by smaller offshore sources, the contribution of the inertial acceleration term may be larger, as it is proportional to the square of the frequency, and hence should not be neglected in the simulations.

This tilt effect rapidly decays with distance to the coast, as evidenced by the data and our modelling, but for a given sea level height, the controlling geometrical factor is not only the distance from the site to the coast, but also the extent of the tsunami offshore (size of the loading source). Consequently, one cannot provide a simple rule relating the near-coast oceanic water level to the tilt observed on land, when the spatial extend—or weight—of the tsunami is not well known. However, when the offshore width of the loading area becomes much larger than the distance from the recording site to the coast, the tilt sensitivity to sea level must become less dependent on this offshore width. This is indeed observed for the sensitivity of the Neuquen tilt records to the Iquique tide gauge records for the Maule and the Tocopilla events, and also on the synthetics records computed for a southern Peru earthquake scenario. In the three cases, we find a tilt of 0.005–0.01 μm at 7 km from the coast in response to a sea level amplitude of 10 cm at the coastline. The tilt decays by a factor of 2 or 3 at 30 km from the coast.

With such sensitivity, LBTs and broadband seismometers located within a few tens of kilometres from the coast appear as very powerful instruments for recording, analysing and modelling tsunamis. Moreover, LBTs are less sensitive to the local strain perturbations from pressure and temperature changes.

A particularly interesting feature is the averaging property of such measurements, over oceanic distances expected to scale with the site-to-coast distance, which thus eliminates local, short wavelength fluctuations (locally recorded by tide gauges), often difficult to model. This provides a robust, spatially smoothed image of the oceanic gravity wave. Optimal distances for such in-land 'weighting' of tsunamis could be in the range of 5–15 km, to allow spatial smoothing while keeping a reasonably high sensitivity.

An additional, very valuable advantage of this remote weighting of tsunamis, with respect to direct sea level measurements on the coast, is their safety with respect to potential tsunami destructions along the coast and their absence of saturation even for the largest run-ups.

We showed above that gravimeters and continuous GPS, although less sensitive, might detect large tsunamis (>2 m) when installed very near to the coast. We can add here that borehole strainmeters, often more sensitive and stable than borehole tiltmeters at the periods of minutes to hours, can provide similar, if not better, information on short-period sea level changes. For instance, the 1 cm amplitude of free oscillations of the surface of the gulf of Corinth, in Greece, in the period range of 10–40 min, provides elastic strain signals of 10^{-8} on the 150 m deep strainmeter of the Trizonia island (located on the coastline), more than 10 times above the noise level (Bernard *et al.* 2004). The increasing number of broadband seismometers, sometimes completed with high-resolution tiltmeters and borehole strainmeters, covering the first tens of kilometres along coastlines may thus provide very valuable records for studying tsunamis, in complement to tide gauges. In case of absence or failure of tide gauges, they may also help study past tsunamis since the 1980s, when new, high-resolution digital seismic instruments began to be deployed.

An important application to be carefully investigated in future studies concerns the early detection of the tsunami arrival, before it reaches the monitored coastal region. Based on the observation for the Maule event and on a realistic simulation for an event in southern Peru, we showed that it is indeed possible to detect a large tsunami wave (1 m high and more) 10–20 min before its arrival at the coastal

site of interest, with instruments having a resolution level of 10^{-9}–10^{-8} radians in tilt (equivalent to 10^{-8}–10^{-7} m s^{-2} in horizontal acceleration) in the period range of minutes to hours. Incidentally, due to their lower noise level in this range, LBTs may provide more appropriate records than standard borehole tiltmeters (Boudin *et al.* 2008). Correlating and modelling tilt records at various sites along the coast may thus constrain the locations, extent and amplitude of tsunamis. However, this will require careful studies, as the perturbing effect of the seismic waves from the main shock should be carefully identified and eliminated from the records through adequate filtering and windowing.

In conclusion, the analysis and successful modelling of LBTs and broadband seismometers records of large tsunamis in northern Chile has demonstrated the ability of near-coast instruments to weight and constrain tsunami gravity waves. The latter have a typical influence, 5 km inland, of the order of 10^{-8} rad for 10 cm of sea level change. The physical mechanism that produces the tilt appears to be dominated by elastic deformation due to oceanic loading, but the gravitational attraction and to a lesser extent horizontal inertial acceleration can contribute to more than 20 per cent of the signal. Consequently, such measurements may contribute to feed inversion of tsunami data, and thus may help constraining sources of past and future tsunamis. Our analysis also shows the potential of this approach for contributing to the possible detection and quantification of an incoming, large tsunami 10–20 min before it reaches the coast nearest to the monitoring instrument.

ACKNOWLEDGEMENTS

This work and the data have been supported by the IPOC network (CNRS-INSU/GFZ/DGF-Santiago) available on the websites:

[1] http://geoscope.ipgp.fr/index.php/en/data/archived-data/data-access.
[2] http://geofon.gfz-potsdam.de/waveform/.
We have used too the data of the 'Servicio Hidrográfico y Oceanográfico de la Armada' (SHOA) available on the website:
[3] http://www.ioc-sealevelmonitoring.org.

We specially thank the 'Universidad Arturo Prat' and the departamento de Geofisica de universidad de Chile for their support to the project, and in particular for the use of the mine Santa Rosa station. Finally, we thank all the help given by Renato Tapia for built of the IPOC stations: solar panels, niches and armour-plated doors protected.

REFERENCES

Agnew, D.C., 1986. Strainmeters and tiltmeters, *Rev. Geophys.,* **24,** 579–624.

Angermann, D., Klotz, J. & Reigber, C., 1999. Space-geodetic estimation of the Nazca-South America Euler vector, *Earth planet. Sci. Lett.,* **171**(3), 329–334.

Bernard, P. *et al.*, 2004. Continuous strain and tilt monitoring on the Trizonia island, Rift of Corinth, Greece, *C. R. Geosci.,* **336,** 313–323.

Berndt, C., Brune, S., Nisbet, E., Zschau, J. & Sobolev, S.V., 2009. Tsunami modeling of a submarine landslide in the Fram Strait, *Geochem. Geophys. Geosyst.,* **10,** Q04009, doi:10.1029/2008GC002292.

Blum, P.A. & Hatzfeld, D., 1970. Etude régionale de l'influence océanique sur l'inclinaison: premiers résultats à la station de Moulis, in *Proceedings of 6th Int. Symp. On Earth Tides,* Strasbourg, pp. 102–105.

Boudin, F., Bernard, P., Longuevergne, L., Florsch, N., Larmat, C., Blum, P.-A., Kammenthaler, M. & Vincent, T., 2008. A silica long base tiltmeter with high stability and resolution, *Rev. Sci. Instrum.,* **79,** 034502, doi:10.1063/1.2829989.

Chlieh, M., de Chabalier, J.B., Ruegg, J.C., Armijo, R., Dmowska, R., Campos, J. & Feigl, K.L., 2004. Crustal deformation and fault slip during the seismic cycle in the North Chile subduction zone, from GPS and InSAR observations, *Geophys. J. Int.,* **158,** 695–711.

Comte, D. & Pardo, M., 1991. Reappraisal of great historical earthquakes in the northern Chile and southern Peru seismic gaps, *Nat. Hazards,* **4,** 23–44.

Darwin, C., 1851. *Geological Observations on Coral Reefs, Volcanic Islands and on South America,* Smith, Elder and Co., London, p. 768.

Delouis, B., Nocquet, J.-M. & Vallée, M., 2010. Slip distribution of the February 27, 2010 Mw = 8.8 Maule Earthquake, central Chile, from static and high-rate GPS, InSAR, and broadband teleseismic data, *Geophys. Res. Lett.,* **37,** L17305, doi:10.1029/2010GL043899.

Delouis, B., Pardo, M., Legrand, D. & Monfret, T., 2009. The Mw 7.7 Tocopilla earthquake of 14 November 2007 at the Southern Edge of the Northern Chile seismic gap: rupture in the deep part of the coupled plate interface, *Bull. seism. Soc. Am.,* **99,** 87–94.

Dorbath, L., Cisternas, A. & Dorbath, C., 1990. Quantitative assessment of great earthquakes in Peru, *Bull. seism. Soc. Am.,* **80,** 551–576.

D'Oreye, N. & Zürn, W., 2005. Very high resolution long-baseline water-tube tiltmeter to record small signals from Earth free oscillations up to secular tilts, *Rev. Sci. Instrum.,* **76,** 024501, doi:10.1063/1.1844451.

Elosegui, P., Davis, J.L., Oberlander, D., Baena, R. & Ekstrom, G., 2006. Accuracy of high-rate GPS for seismology, *Geophys. Res. Lett.,* **33,** L11308, doi:10.1029/2006GL026065.

Farrell, W.E., 1972. Deformation of the Earth by surface loads, *Rev. geophys. Space Phys.,* **10,** 761–797.

Fritz, H.M. *et al.*, 2011. Field Survey of the 27 February 2010 Chile Tsunami, *Pure appl. Geophys.,* **168**(11) 1989–2010.

Hébert, H., Heinrich, P., Schindelé, F. & Piatanesi, A., 2001. Far-field simulation of tsunami propagation in the Pacific Ocean: impact on the Marquesas Islands (French Polynesia), *J. geophys. Res.,* **106**(C5), 9161–9177.

IOC, IHO & BODC, 2003. *Centenary Edition of the GEBCO Digital Atlas,* published on CD-ROM on behalf of the Intergovernmental Oceanographic Commission and the International Hydrographic Organization as part of the General Bathymetric Chart of the Oceans, British Oceanographic Data Centre, Liverpool, UK.

Ito, T. & Simons, M., 2011. Probing asthenospheric density, temperature, and elastic moduli below the Western United States, *Science,* **332,** 947–951.

Kostoglodov, V., Bilham, R., Santiago, J.A., Manea, V., Manea, M. & Hernandez, V.R., 2002. Long-baseline fluid tiltmeter for seismotectonic studies of Mexican subduction zone, *Geofisica Int.,* **41**(1), 11–25.

Longuevergne, L., Florsch, N., Boudin, F., Oudin, L. & Camerlynck, C., 2009. Tilt and strain deformation induced by hydrologically active natural fractures: application to the tiltmeters installed in Sainte-Croix-aux-Mines observatory (France), *Geophys. J. Int.,* **178**(2), 667–677.

Nawa, K., Suda, N., Satake, K., Fujii, Y., Sato, T., Doi, K., Kanao, M. & Shibuva, K., 2007. Loading and gravitational effects of the 2004 Indian ocean tsunami at Syowa Station, Antarctica, *Bull. seism. Soc. Am.,* **97**(1A), S271–S278.

Pagiatakis, S.D., 1990. The response of a realistic earth to ocean tide loading, *Geophys. J. Int.,* **103,** 541–560.

Peyrat, S., Madariaga, R., Buforn, E., Campos, J., Asch, G. & Vilotte, J.P., 2010. Kinematic rupture process of the 2007 Tocopilla earthquake and its main aftershocks from teleseismic and strong motion data, *Geophys. J. Int.,* **182,** 1411–1430.

Pino, N.A., Ripepe, M. & Cimini, G.B., 2004. The Stromboli Volcano landslides of December 2002: a seismological description, *Geophys. Res. Lett.,* **31,** L02605, doi:10.1029/2003GL018385.

Plafker, G. & Savage, J.C., 1970. Mechanism of the Chilean earthquake of May 21 and 22 1960, *Geol. Soc. Am. Bull.,* **81,** 1001–1030.

Sahal, A., Roger, J., Allgeyer, S., Lemaire, B., Hébert, H., Schindel, F. & Lavigne, F., 2009. The tsunami triggered by the 21 May 2003 BoumerdÀes-Zemmouri (Algeria) earthquake: field investigations on the French Mediterranean coast and tsunami modelling, *Nat. Hazards Earth Syst. Sci.,* **9,** 1823–1834.

Vergnolle, M., Bouin, M.N., Morel, L., Masson, F., Durand, S., Nicolas, J. & Melachroinos, S.A., 2008. GPS estimates of ocean tide loading in NW-France: determination of ocean tide loading constituents and comparison with a recent ocean tide model, *Geophys. J. Int.*, **173,** 444–458.

Vigny, C. *et al.*, 2011. The 2010 Mw 8.8 Maule Mega-Thrust Earthquake of Central Chile, Monitored by GPS, *Science,* **332,** 1417–1421.

Wenzel, H.-G., 1996. Earth Tide Data Processing Package ETERNA 3.30, Manual ETERNA33. HLP.

Williams, S.D.P. & Penna, N.T., 2011. Non-tidal ocean loading effects on geodetic GPS heights, *Geophys. Res. Lett.,* **38,** L09314, doi:10.1029/2011GL046940.

Yamazaki, Y. & Cheung, K.F., 2011. Shelf resonance and impact of near-field tsunami generated by the 2010 Chile earthquake, *Geophys. Res. Lett.,* **38,** L12605, doi:10.1029/2011GL047508.

Yuan, X., Kind, R. & Pedersen, H.A., 2005. Seismic monitoring of the Indian Ocean tsunami, *Geophys. Res. Lett.,* **32,** L15308, doi:10.1029/2005GL023464.

APPENDIX A

The synthetic horizontal inertial accelerations produced by the horizontal displacements resulting from the predicted elastic load of the tsunami are presented in Fig. A1 (right panel), together with the displacements (left panel), for the N (top) and E (bottom) components. The various curves in each plot correspond to varying distances between the site and the coastline, at the latitude of Neuquen. The results are that these inertial accelerations remain at all time at least two orders of magnitude smaller than the horizontal accelerations recorded by the instruments so that the latter are dominated by the horizontal component of the earth gravity (due to tilt) and the gravitational attraction from the water mass.

APPENDIX B

The comparison of the records from the reference LVC station (137 km far from the coast) to the records of the near-coastal stations is presented in Fig. B1. It shows that a significant part of the signal at periods shorter than 800 s is of seismic origin. In the following hours, after the passage of the direct surface waves (first 15 min), it shows the arrival of successive Rayleigh and Love waves. All these signals show a similar amplitude and no significant phase shift (smaller than 20 s), ruling out the possibility of a tsunami-induced signal.

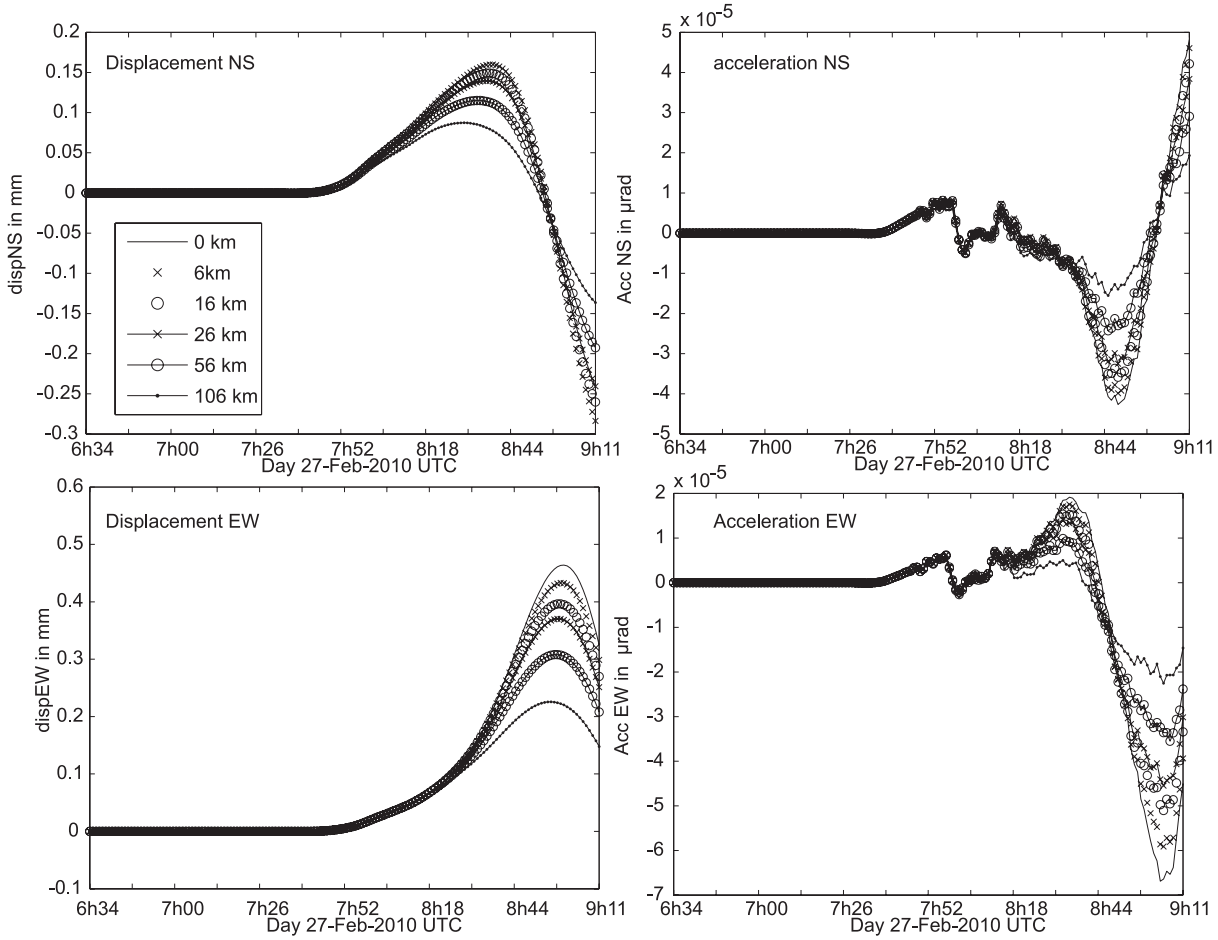

Figure A1. Theoretical horizontal displacement and acceleration due to the 2010 Maule tsunami. (Left) NS (top) and EW (bottom) displacement. (Right) NS (top) and EW (bottom) acceleration. The various curves correspond to different distances from the coast at the latitude of Iquique (0, 6, 16, 26, 56 and 108 km).

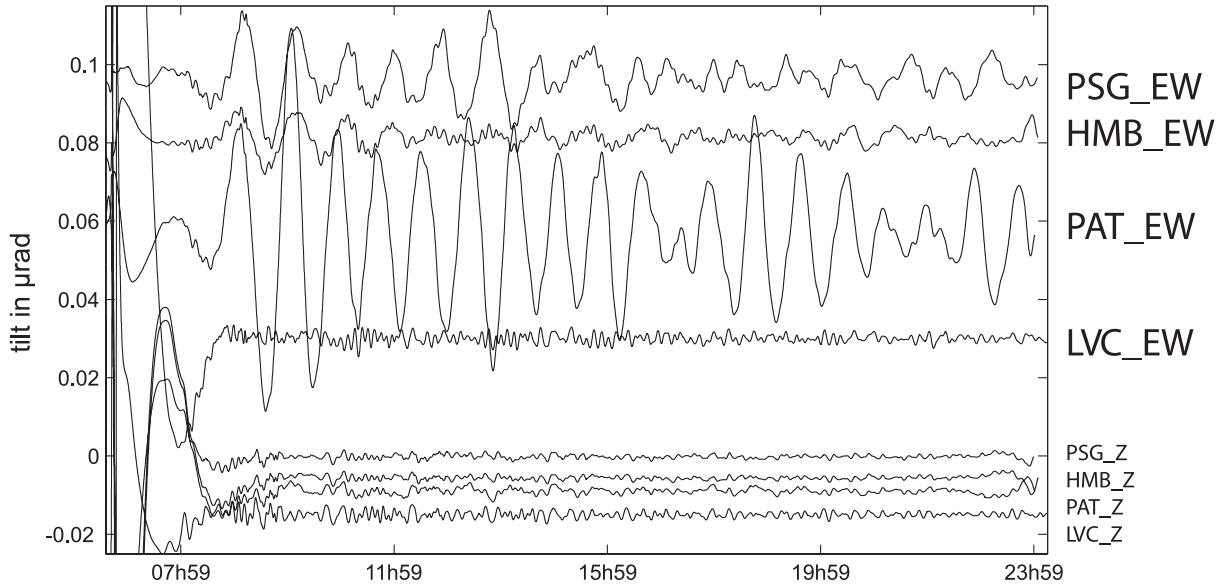

Figure B1. Bandpass filtered acceleration (horizontal and vertical) at 4 STS2 sites for the 2010 Maule earthquake. At the top EW and Z accelerations at PSG, HMB, PAT and LVC. Note the absence of the tsunami-induced long periods on the horizontal component of LVC and the similarity of all vertical components.